

# Dynamic Rupture Scenarios of the Cascadia Megathrust based on Interseismic Locking Models

Yuk Po Bowie Chan<sup>1</sup>, Suli Yao<sup>2</sup>, and Hongfeng Yang<sup>1</sup>

<sup>1</sup>The Chinese University of Hong Kong

<sup>2</sup>Chinese University of Hong Kong

February 1, 2023

## Abstract

The Cascadia subduction zone in the Pacific Northwest has well-documented geological records of megathrust earthquakes with the most recent Mw 9 rupture occurring in 1700 A.D. The paleoseismic observations suggest that Southern Cascadia is mature for future earthquakes since the last event. Consequently, it is crucial to investigate the potential rupture scenarios. Various interseismic locking models are developed along Cascadia, including offshore uncertainties and different material assumptions. Although they all share similar moment deficits, whether future earthquakes may rupture the entire margin or be segmented, as found in the paleoseismic records, remains unknown. Accordingly, we aim to investigate: (1) possible rupture segmentation patterns, (2) whether south Cascadia can host margin-wide ruptures, and (3) whether the existing locking models suggest similar future rupture scenarios. We estimate the stress distribution constrained by the locking models from static calculation and discover that they lead to different stress distributions, indicating distinct seismic potentials despite their similar moment deficits. Our dynamic rupture scenarios show that the south can generate both segmented ruptures ( $> Mw 7.3 - 8.4$ ) and margin-wide ruptures ( $> Mw 8.6$ ) depending on hypocenter locations. The extent of Schmalzle-based segmented scenarios matches the proposed historical segmented events, and the margin-wide scenarios are well consistent with the coastal subsidence records of 1700 A.D. Therefore, we propose that three high-slip trench-breaching patches are sufficient for reproducing historical subsidence records. Our reasonable dynamic simulations can be applied in future studies for assessing seismic and tsunami hazards, and also serve as a comparison for non-trench-breaching scenarios.

## Hosted file

953498\_0\_art\_file\_10587646\_rz0fz8.docx available at <https://authorea.com/users/575014/articles/618470-dynamic-rupture-scenarios-of-the-cascadia-megathrust-based-on-interseismic-locking-models>

# Dynamic Rupture Scenarios of the Cascadia Megathrust based on Interseismic Locking Models

Yuk Po Bowie Chan<sup>1</sup>, Suli Yao<sup>1</sup>, Hongfeng Yang<sup>1,2</sup>

<sup>1</sup>Earth and Environmental Sciences Programme, The Chinese University of Hong Kong, Hong Kong, China, <sup>2</sup>Shenzhen Research Institute, The Chinese University of Hong Kong, Shenzhen, China

Correspondence to:

H. Yang,

[hyang@cuhk.edu.hk](mailto:hyang@cuhk.edu.hk)

Key Points:

- We conduct 3D dynamic rupture simulations for the future possible scenarios in Cascadia with constraints from interseismic locking models
- Application of different hypocenter locations reveals rupture segmentation and rupture directivity
- Our dynamic rupture scenarios have reasonably consistent segmentation extents and coastal subsidence patterns with paleoseismic observations

Abstract

The Cascadia subduction zone in the Pacific Northwest has well-documented geological records of megathrust earthquakes with the most recent Mw 9 rupture occurring in 1700 A.D. The paleoseismic observations suggest that Southern Cascadia is mature for future earthquakes since the last event. Consequently, it is crucial to investigate the potential rupture scenarios. Various interseismic locking models are developed along Cascadia, including offshore uncertainties and different material assumptions. Although they all share similar moment deficits, whether future earthquakes may rupture the entire margin or be segmented, as found in the paleoseismic records, remains unknown. Accordingly, we aim to investigate: (1) possible rupture segmentation patterns, (2) whether south Cascadia can host margin-wide ruptures, and (3) whether the existing locking models suggest similar future rupture scenarios. We estimate the stress distribution constrained by the locking models from static calculation and discover

34 that they lead to different stress distributions, indicating distinct seismic potentials despite their  
35 similar moment deficits. Our dynamic rupture scenarios show that the south can generate both  
36 segmented ruptures ( $> M_w 7.3 - 8.4$ ) and margin-wide ruptures ( $> M_w 8.6$ ) depending on  
37 hypocenter locations. The extent of Schmalzle-based segmented scenarios matches the  
38 proposed historical segmented events, and the margin-wide scenarios are well consistent with  
39 the coastal subsidence records of 1700 A.D. Therefore, we propose that three high-slip  
40 trench-breaching patches are sufficient for reproducing historical subsidence records. Our  
41 reasonable dynamic simulations can be applied in future studies for assessing seismic and  
42 tsunami hazards, and also serve as a comparison for non-trench-breaching scenarios.

43

#### 44 Plain Language Summary

45

46 Earthquakes occur when the shear stresses on a fault overcome the frictional resistance to cause  
47 a sudden slip. In subduction zones, the tectonic plates converge and the stresses accumulate at  
48 the contact between the plates. As more stresses accumulate on the interface, great earthquakes  
49 are possible. Although there are no significant earthquakes ( $> M_w 8$ ) since 1700 A.D., the  
50 Cascadia subduction zone in the Pacific Northwest is known to have historical  $M_w 9$   
51 earthquakes based on geological studies. Interseismic locking models describe the relative  
52 motion of the fault. For instance, 1 means fully locked where the two sides do not move against  
53 each other, thus accumulating stress. We infer stress distributions from interseismic locking  
54 models and conduct 3D dynamic simulations based on the stresses to explore possible future  
55 earthquake extents. Our results demonstrate various scenarios, including single-segment ( $>$   
56  $M_w 7.3 - 8.2$ ), multiple-segments ( $> M_w 8.2 - 8.4$ ), and full-margin ruptures ( $> M_w 8.6$ ).  
57 Most of these scenarios are consistent with geological records, suggesting our scenarios are  
58 reasonable future earthquake estimates.

59

#### 60 1. Introduction

61

62 The Cascadia subduction zone is known to host great megathrust earthquakes as large as moment  
63 magnitude ( $M_w$ ) 9 (Wang and Tréhu, 2016; Walton et al., 2021). Based on paleoseismic records  
64 (Long and Shennan 1998; Kelsey et al. 2005; Goldfinger et al. 2012; Engelhart et al. 2015), the  
65 average recurrence interval of these events is about 500 yrs but with large variations. It has been  
66 over 322 years since the latest great earthquake, an  $M \sim 9$  margin-wide rupture in A.D. 1700

67 accompanied with a large, trans-Pacific tsunami (Atwater and Hemphill-Haley 1997; Goldfinger  
68 et al. 2012, 2017; Satake et al., 2003). Modern interseismic geodetic observations indicate  
69 accumulation of energy along almost the entire Cascadia margin towards a future earthquake  
70 (Flück et al., 1997; Wang et al., 2003; Burgette et al., 2009; McCaffrey et al., 2013; Schmalzle  
71 et al. 2014; Pollitz and Evans, 2017; Li et al. 2018; Michel et al. 2019; Lindsey et al. 2021).

72

73 One challenge in seismic hazard assessment at Cascadia is estimating the potential of rupture  
74 segmentation along the megathrust. There are questions regarding whether past events were  
75 predominantly full-margin ruptures or sequences of smaller ruptures that were too closely  
76 spaced in time to be resolved by paleoseismic records (Wang et al., 2013; Atwater et al. 2014;  
77 Frankel et al. 2015). Along-strike heterogeneities in megathrust and crustal structure are thought  
78 to have the potential to cause rupture segmentation in various parts of the margin (Tréhu et al.,  
79 2012; Wang and Tréhu, 2016; Watt and Brothers, 2021). Based on the interpretation of offshore  
80 turbidity records, megathrust earthquakes occurred more frequently in southern Cascadia,  
81 especially south of Cape Blanco (Goldfinger et al., 2017). The average recurrence interval is  
82 inferred to increase from around 200 years in the south to around 300 years in the central  
83 segment and 400-500 years in the north (Witter et al., 2012; Goldfinger et al. 2017). If the  
84 A.D.1700 event was a full-margin rupture as inferred by Satake et al. (2003), then at present the  
85 short-recurrence southern segment is statistically expected to be more ready for the next rupture.  
86 The first scientific question we address in this study is whether the next large earthquake is more  
87 likely a full-margin rupture or to be confined in the south.

88

89 Dynamic rupture scenarios based on interseismic locking models can contribute to estimating  
90 the magnitude, rupture extent, and potential segmentation of future earthquakes (Yang et al.,  
91 2019a; Li and Liu, 2021; Ramos et al., 2021; Yao and Yang, 2022). For instance, Yang et al.  
92 (2019a) derived dynamic scenarios for the Costa Rica subduction zone by using interseismic  
93 locking models to derive the initial stress of the megathrust prior to the rupture and were able to  
94 explain the rupture extent and magnitude of the 2012 Nicoya Mw 7.6 earthquake. Using a similar  
95 approach, Ramos et al. (2021) conducted dynamic rupture simulations for Cascadia with the  
96 initial stress based on the interseismic locking model of Schmalzle et al. (2014). By nucleating  
97 ruptures from a high-stress location either in the south or in the north, they obtained scenarios of  
98 margin-wide rupture. Li and Liu (2021) conducted quasi-dynamic numerical simulation of  
99 long-term fault behavior in Cascadia. They inferred fault rate-state friction stability from

100 interseismic locking models (Schmalzle et al. 2014; Burgette et al., 2009). They found that  
 101 whether the rupture was full-margin depended on what locking model was used.

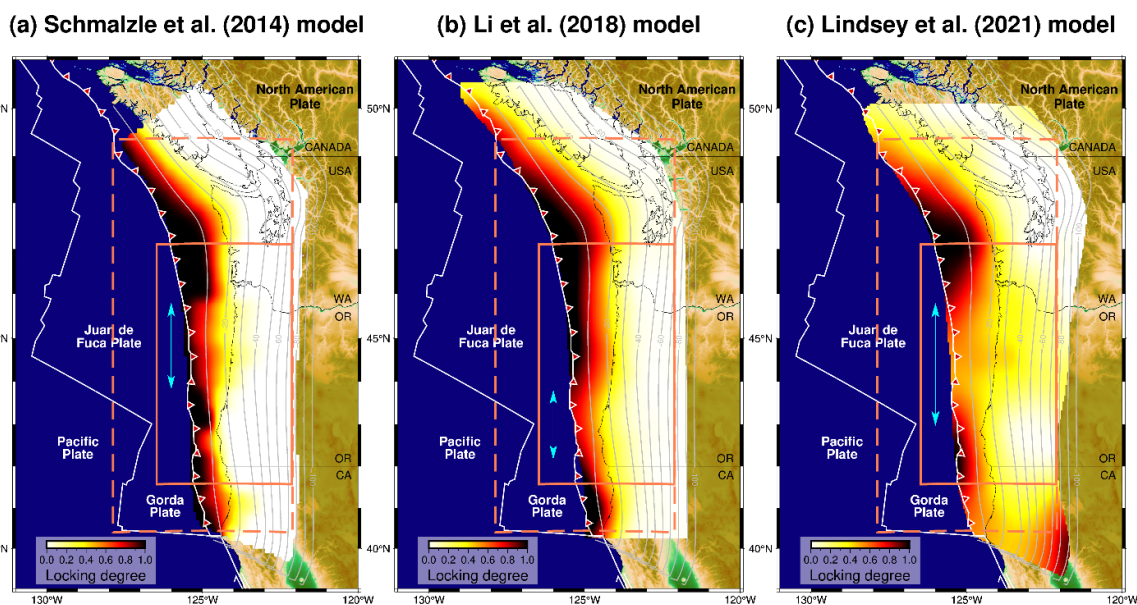
102

103 Besides rupture extent and earthquake magnitude, the effect of rupture directivity on ground  
 104 motion should be further investigated using dynamic rupture simulations. It is well understood  
 105 that, with a heterogeneous initial stress distribution along the fault, different hypocenter  
 106 locations can lead to different rupture directivities (Yang et al., 2019b; Yao and Yang, 2022).  
 107 Even with a similar rupture extent, a different rupture directivity leads to a very different pattern  
 108 of ground motion intensity (Yao and Yang, 2022). Therefore, the second scientific question we  
 109 address in this study is how hypocenter location controls rupture directivity to impact ground  
 110 motion.

111

112 To investigate the above questions, we carry out dynamic rupture simulation to obtain  
 113 self-consistent rupture scenarios. We consider different Cascadia megathrust locking models  
 114 (Figure 1), namely those by Schmalzle et al. (2014), Li et al. (2018), and Lindsey et al. (2021).  
 115 Our research aims to derive rupture scenarios originating from South Cascadia. Assuming the  
 116 same stress accumulation time, we investigate the role of stress distribution and hypocenter  
 117 location in producing possible segmentation patterns and ground motion patterns. We further  
 118 compare the rupture scenarios with the proposed segmented paleoearthquakes as well as  
 119 coseismic subsidence amplitudes.

120



122 Figure 1. Interseismic locking models for CSZ. (a) Model from Schmalzle et al. (2014). (b)  
123 Model from Li et al. (2018). (c) Model from Lindsey et al. (2021). Coral dashed line: our static  
124 calculation domain. Coral solid line: our dynamic simulation domain. Cyan arrow: central  
125 creeping segments.

126

127 2. Interseismic locking models of the Cascadia megathrust

128

129 Since solutions for the inversion of geodetic measurements are nonunique, different  
130 assumptions are applied in deriving interseismic locking models, governing the smoothness of  
131 slip distribution and the degree of locking at the trench (McCaffrey et al., 2013; Schmalzle et al.  
132 2014; Pollitz and Evans, 2017; Li et al. 2018; Michel et al. 2019; Lindsey et al. 2021). Here we  
133 summarize the three locking models adopted in this work, all derived by inverting land-based  
134 GNSS observations (Figure 1). Although Cascadia does not have a geomorphological trench  
135 because of the thick sediment cover, we refer to the deformation front as the “trench” in the  
136 following discussion for wording convenience.

137

138 Because land-based GNSS measurements cannot resolve the locking state of the shallowest  
139 portion of the megathrust which is far offshore, Schmalzle et al. (2014), following McCaffrey  
140 et al. (2013), proposed two models of opposite, prescribed near-trench locking states which fit  
141 the GNSS data equally well. One model assumes full locking at the trench with the locking  
142 degree monotonically decreasing downdip following the Gamma function designed by Wang et  
143 al. (2003) (Gamma model). The other model assumes a Gaussian-like locking distribution so  
144 that creeping occurs at the trench and full locking occurs farther downdip (Gaussian model).  
145 Creeping of the shallowest part of the fault may occur in a transient fashion such as during  
146 earthquake afterslip or slow slip events but is unlikely a sustained behavior over the  
147 interseismic period (Wang and Dixon, 2004; Wang, 2007). Thus, in this study we only use the  
148 Gamma model, referred to as the Schmalzle model hereafter (Figure 1a).

149

150 Following the explanation of Wang and Dixon (2004) and Wang (2007), Lindsey et al. (2021)  
151 included in their locking model the effect of stress shadowing in which a frictionally unlocked  
152 shallow segment of the fault may have little motion because of the neighboring frictionally  
153 locked patches immediately downdip. Although stress shadowing is explicitly invoked, the  
154 kinematic behavior of the megathrust in this model is similar to that described by the

155 aforementioned Gamma model. The difference in inversion results is caused mainly by  
156 assumed inversion parameters that constrain slip deficit distribution. In this study, we use their  
157 best-fit locking model, referred to as the Lindsey model (Figure 1c).

158

159 The above two locking models assume an elastic Earth, but the real Earth is viscoelastic, and  
160 viscoelastic stress relaxation plays an important role not only in postseismic but also  
161 interseismic deformation (Wang et al., 2012). To address this effect, Pollitz and Evans (2017)  
162 and Li et al. (2018) inverted Cascadia interseismic geodetic data based on analytical solutions  
163 and finite element models, respectively. Li et al. (2018) constructed many locking models that  
164 fit the geodetic data equally well. Here we only use their “preferred” locking model, referred to  
165 as the Li model (Figure 1b).

166

167 Because of the lack of near-field, seafloor geodetic constraints, all these models suffer from a  
168 high degree of nonuniqueness and thus contain large errors. By using these models to design  
169 initial fault stress distribution, we do not intend to construct a “correct” dynamic rupture model.  
170 Instead, we use these models to explore how different initial stress distributions may affect the  
171 rupture process. As such, these models may be considered as ad-hoc to each other. Improved  
172 understanding of the dynamic rupture process will help the design of kinematic rupture models  
173 for the purpose of probabilistic seismic hazard analyses and the appraisal of model uncertainties.  
174 We think the three models shown in Figure 1 adequately represent the range of assumptions used  
175 in constructing Cascadia megathrust locking models by different research groups in terms of  
176 Earth rheology, near-trench locking state, and smoothness of slip deficit distribution. Since stress  
177 accumulation is mostly determined by the spatial gradient of the locking distribution and the  
178 major first-order features of active faulting could be governed by the spatial gradients of stress  
179 (Nur, 1978), it is important to ask whether the slip deficit heterogeneities in these locking models  
180 can lead to consistent rupture scenarios.

181

### 182 3. Method and model parameter

183

184 We use open-source finite-element code PyLith which is developed for dynamic and quasi-static  
185 simulations of crustal deformation (Aagaard et al., 2017a). Input parameters for our dynamic  
186 simulation include fault geometry, material properties, initial stresses ( $\tau_0$ ), and fault frictional  
187 law parameters (Harris et al., 2018).

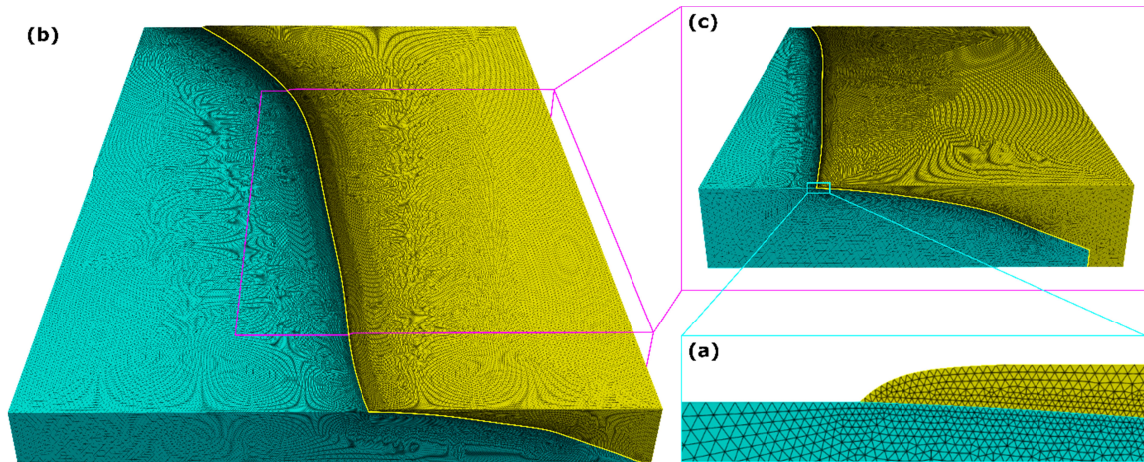
188

## 189 3.1 Megathrust geometry and mesh

190

191 We adopt the Cascadia megathrust model of McCrory et al. (2004), which has a smoothly  
 192 curved geometry starting from a 5 km depth below sea level and use an exponential curve to  
 193 approximate the shape of the upper plate near the trench as shown in Figure 2a.

194



195

196 Figure 2. 3D model configuration. (a) Mesh geometry near the trench – continental block edge  
 197 approximated with an exponential curve away from the trench. (b) Finite element mesh for  
 198 static calculation with two model units: oceanic block (cyan) and continental block (yellow). (c)  
 199 Finite element for the dynamic simulations.

200

201 We generate two 3D tetrahedral meshes for Cascadia using geometry and mesh generation  
 202 software CUBIT (Blacker et al., 2016) to accommodate scientific purposes and computational  
 203 cost. Both meshes each consists of two model units - the oceanic block and the continental block.  
 204 We use the larger one of the two meshes, extending from 40.5°N to 49°N covering the whole  
 205 megathrust (Figure 2) to calculate stress distribution from locking models. We apply a  
 206 coordinate transformation to fix the origin at -129°E, 39°N. This larger mesh extends 970 km,  
 207 600 km, and 75 km in the strike, strike-normal, and depth dimensions, respectively (Figure 2b).  
 208 The element size on the fault is 500 m above 35 km depth for the major locked zone and  
 209 gradually increases downdip.

210

211 For computational efficiency, we use the smaller one of the two meshes, extending from  
 212 41.5°N to 47°N, to conduct dynamic rupture simulation in our area of focus. We are focused

213 mainly on the scenarios of rupture initiation in the south and on the effect of the central  
214 segment. Geological evidence of ruptures limited to northern Cascadia is elusive (Petersen et al.  
215 2014), suggesting that ruptures breaking the northern segment might eventually develop into  
216 margin-wide ruptures. This is consistent with the higher stress accumulation in the north  
217 provided by most locking models (Burgette et al. 2009; McCaffrey et al. 2013; Schmalzle et al.  
218 2014; Pollitz and Evans, 2017; Li et al. 2018; Michel et al. 2019; Lindsey et al. 2021) as well  
219 as the dynamic simulation results from Ramos et al. (2021). The small mesh covers the entire  
220 southern and central Cascadia, extending 600 km, 420 km, and 95 km in the strike,  
221 strike-normal, and depth dimensions, respectively (Figure 2c). The element size is 500 m above  
222 50 km depth and gradually increases further downdip.

223

224 To minimize potential artefacts due to mesh boundaries, we extend the small mesh for the  
225 dynamic simulation to 95 km depth and even deeper than the larger mesh for static calculation  
226 by 20 km. In comparison, interseismic locking occurs mostly shallower than 30 km depth  
227 (Figure 1) and, to be further explained in sections 3.3 and 4.1, the model-predicted rupture  
228 propagation does not extend far beyond this depth because of lack of inferred interseismic  
229 stress built-up farther downdip. As will be shown section 4.2, none of our simulations features  
230 rupture deeper than 50 km depth.

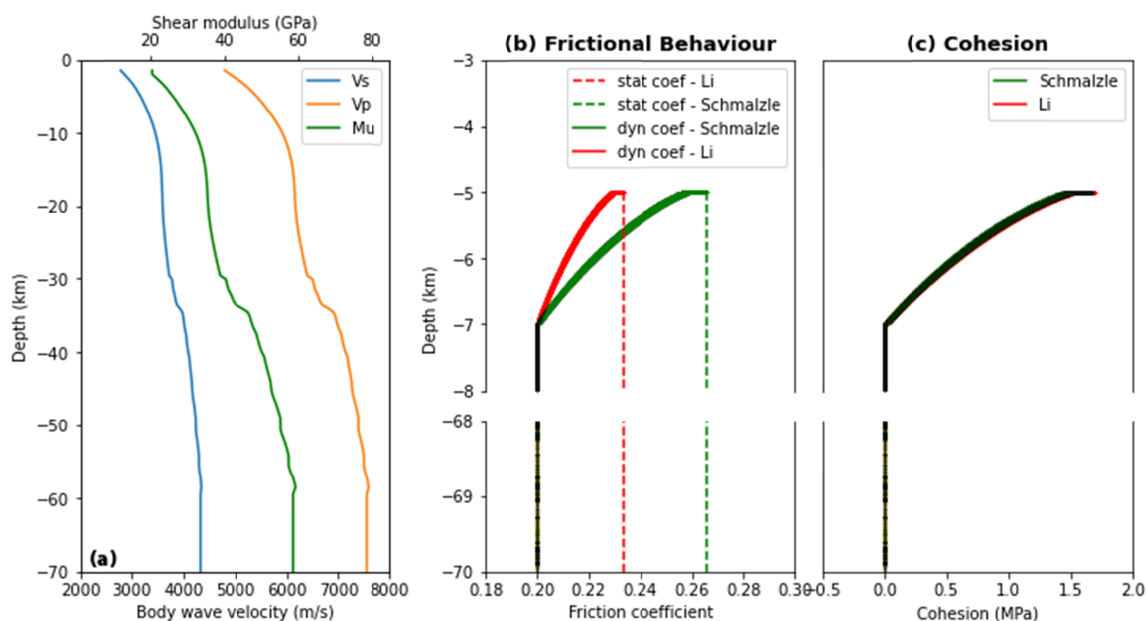
231

### 232 3.2 Material Properties

233

234 Similar to most other dynamic rupture models, we assume an elastic Earth and apply absorbing  
235 conditions to all boundaries except the free surface at the top. The material property structure is  
236 based on the 3D Community Velocity Model (CVM) of Cascadia (Stephenson et al. 2017) in  
237 which the body wave velocities of the oceanic block are approximately 30% higher than the  
238 continental block. The density is calculated from p-wave velocity based on the empirical  
239 relationship of Brocher (2005). We have tested two different material property structures in  
240 order to see how they affect the dynamic rupture process. One model is referred to as the 1-D  
241 velocity model, in which the material properties of the continental block are applied to the whole  
242 mesh. Another model is referred to as the bi-material velocity model, where material properties  
243 of both continental and oceanic blocks are considered (Figure S1). The two structures lead to  
244 very similar rupture scenarios. Between the two test models shown in Figure S2, the moment

245 magnitude differs only by 0.01 (Figure S2). Hence, we use the 1-D velocity structure for the rest  
 246 of our dynamic simulations (Figure 3a).  
 247



248  
 249 Figure 3. Depth-dependent parameters for dynamic rupture simulations. (a) 1-D velocity model  
 250 calculated from Stephenson et al. (2017) and shear modulus. (b) Dynamic and static  
 251 coefficients which remain constant below 7 km depth. (c) Cohesion, remaining constant below  
 252 7 km depth. Note that it appears dark because the two curves are overlapping.

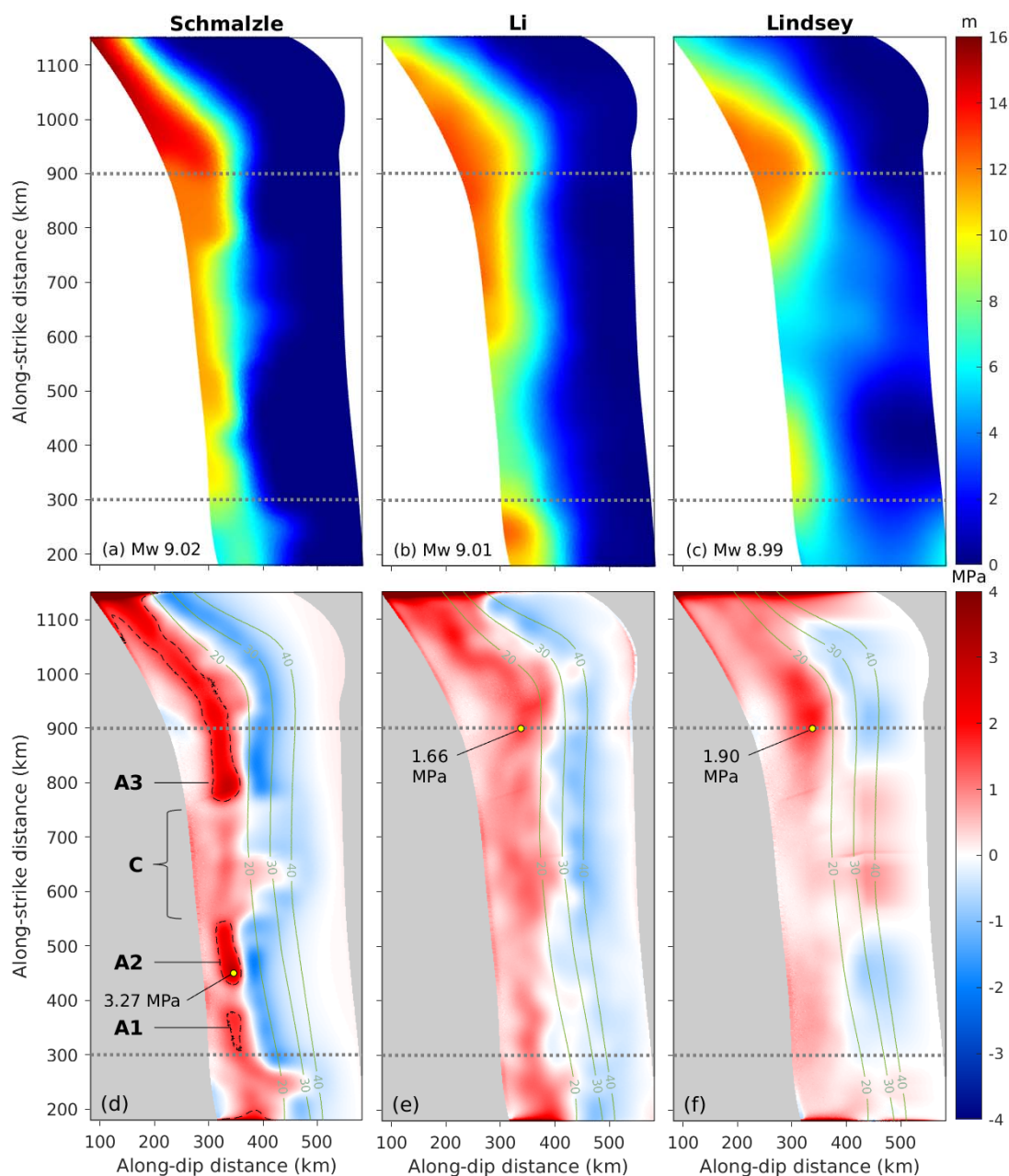
253

### 254 3.3 Stress accumulation and initial stress on the megathrust

255

256 Following previous studies (Yang et al., 2019b; Ramos et al., 2021), we assume that the slip  
 257 deficit has been continuously accumulated since the A.D.1700 earthquake. There are  
 258 uncertainties associated with this assumption because there are no observational constraints on  
 259 whether medium size earthquakes or significant creep occurred in the seismogenic depth range  
 260 of the megathrust after 1700 but before the instrumental era. Upon interpreting GNSS velocity  
 261 variations, Materna et al. (2019) proposed temporal variations in megathrust locking in  
 262 southernmost Cascadia updip of the ETS zone associated with stress perturbations due to  
 263 offshore M6+ earthquakes in the incoming oceanic plate. We do not include these complicated  
 264 temporal variations in our calculation of slip deficit because neither the uniqueness of the  
 265 GNSS data interpretation nor the physical mechanism of the proposed variations are well  
 266 understood.

267



268

269 Figure 4. Slip deficit and stress change. (a) – (c): Total slip deficit with a uniform stress  
 270 accumulation time of 320 years. Dotted lines: the boundaries of the dynamic simulation  
 271 domain. (d) – (f): Dip component of the stress build-up caused by the slip deficit in (a) – (c).  
 272 Dotted lines: the boundaries of the dynamic simulation domain. Yellow dots: the point of  
 273 highest stress change magnitude within the dynamic modelling domain. Dashed lines in (d):  
 274 1.5 MPa stress contours. A1, A2, and A3 refer to the stress asperities while C marks the  
 275 creeping segment extent.

276

277 With the interseismic locking distribution assumed to be time-independent, the slip deficit at  
278 present (Figures 5a – 5c) is simply the product of the subduction rate, slip deficit rate as a  
279 fraction of the subduction rate as given by the locking models (i.e., the locking degree in  
280 Figure 1), and the time since the A.D. 1700 great earthquake. In an elastic model, the  
281 incremental stress associated with the accumulation of this slip deficit can be readily  
282 determined from the slip deficit distribution (similar to the determination of static stress drop  
283 from coseismic slip distribution) (Figures 5d – 5f). Following Yang et al. (2019b) and Ramos  
284 et al. (2021), we assume that this incremental stress solely propels the next megathrust rupture  
285 (Figure 4), which implies that the “base level” of the fault stress plays no role, that is, whether  
286 the A.D.1700 event feature complete or partial stress drop is unimportant. It also means that  
287 the spatial heterogeneity of the fault stress distribution just after that earthquake is unimportant.  
288 This assumption is obviously a leap of faith, but it is theoretically consistent with the  
289 slip-weakening friction law invoked in our modelling which will be explained in section 3.4,  
290 and it makes it operationally possible to derive initial fault stress from interseismic locking  
291 models. Note that the incremental stress derived from one of locking models shown in Figures  
292 1c and 5c occurs far deeper than the commonly assumed seismogenic depth limit of around 30  
293 km in some areas along the margin (Figure 4f). To confine seismic rupture within a reasonable  
294 depth range, we use a cosine function to taper the fault stress in this model to zero from 35 km to  
295 75 km depth (Figure 4f).

296

297 Effective normal stress is the normal stress minus pore fluid pressure. For simplicity, we  
298 assumed as a uniform effective normal stress of 50 MPa on the entire megathrust regardless of  
299 how the shear stress varies along the fault. This low effective normal stress is based on the  
300 notion of very high pore fluid pressurization at depths as inferred for global subduction zones  
301 (Saffer and Tobin, 2011). For example, given an average rock density  $2500 \text{ kg/m}^3$ , an effective  
302 normal stress 50 MPa at depth 20 km requires pore fluid pressure about 90% of the lithostatic  
303 pressure. There is no reason against other small values such as 30 or 60 MPa, and the lack of  
304 depth dependence is for the numerical convenience with little observational support.  
305 Nonetheless, the number 50 MPa we use is a typical value over the velocity-weakening region  
306 which is often used in earthquake simulation studies (Lapusta and Liu, 2009; Michel et al., 2017;  
307 Yang et al., 2019a).

308

309 Cascadia is well-known for Episodic Tremor and Slip (ETS) events (Rogers and Dragert, 2003).  
 310 Gao and Wang (2017) suggest that although the effective normal stress in the ETS region is  
 311 exceptionally low because of near-lithostatic fluid pressure, the ETS zone is rheological  
 312 separated from the seismogenic zone and thus is not involved in dynamic rupture. As will be  
 313 shown in section 4.2, in our models the rupture is arrested before reaching the ETS zone without  
 314 additional constraints, which is consistent with the notion of Gao and Wang (2017).

315

316 Based on findings of high-rate friction experiments (e.g., Di Toro et al., 2011), we set a dynamic  
 317 friction coefficient of 0.2 (i.e., dynamic stress level of 10 MPa) for the fault below 7 km and  
 318 assume it to be constant. The southern Cascadia material for the frontal thrust is  
 319 velocity-weakening while the northern Cascadia material is velocity-strengthening  
 320 (Stanislawski et al., 2022). For simplicity, we assume that the frontal thrust is neutrally stable by  
 321 increasing the dynamic coefficient linearly to the static coefficient levels of 0.2656 and 0.2332  
 322 for Schmalzle and Li models respectively (Figure 3b and Table 1) from 7 km updip to 5 km depth.  
 323 The initial stress prior to the dynamic rupture is the sum of the dynamic stress and the  
 324 interseismic stress accumulation inferred from the locking models.

325

326 **Table 1** Model parameters in dynamic rupture simulations

Fault parameter	Schmalzle model	Li model
Static friction coefficient, $f_s$ (yield strength/ $\sigma_n$ )	0.2656	0.2332
Dynamic friction coefficient, $f_d$ (dynamic stress/ $\sigma_n$ )	0.2	0.2
Effective normal stress, $\sigma_n$ (MPa)	50	50
Critical weakening distance (m)	0.6, 1	0.6, 1

327

### 328 3.4 Fault frictional law and resolution test

329

330 The fault is assumed to be governed by the linear slip-weakening law (Ida, 1972) in which fault  
 331 shear stress  $\tau_f$  is given by (Aagaard et al., 2017b),

$$\tau_f = \begin{cases} \tau_c - (\mu_s - (\mu_s - \mu_d) \frac{d}{d_c}) \tau_n & d \leq d_c \text{ and } \tau_n \leq 0 \\ \tau_c - \mu_d \tau_n & d > d_c \text{ and } \tau_n \leq 0 \\ 0 & \tau_n > 0 \end{cases} \quad (1)$$

332

333 where  $\mu_s$  is the static friction coefficient,  $\mu_d$  is the dynamic friction coefficient,  $d_c$  is the  
 334 slip-weakening distance,  $\tau_n$  is the effective normal stress,  $\tau_c$  is the cohesive stress, and  $d$  is the slip  
 335 distance. The frictional resistance ( $\tau_f$ ) decreases linearly with increasing fault slip when  $d < d_c$   
 336 but stays constant when  $d > d_c$ . It should be emphasize that, according to the slip-weakening  
 337 law, the rupture behavior is controlled by the difference between yield stress and initial stress  
 338 instead of the absolute stress level.

339

340 We set the yield stress, which is the product of static friction coefficient and normal stress, to be  
 341 uniformly 0.01 MPa above the maximum initial shear stress on the fault within the dynamic  
 342 modelling domain (Figure 3b and Table 1). For example, the highest interseismic stress  
 343 accumulation within the region of dynamic modelling in accordance with the Schmalzle slip  
 344 deficit distribution is 3.27 MPa (Figure 4e) which, with the uniform dynamic stress 10 MPa,  
 345 gives the highest initial stress  $3.27 + 10 \text{ MPa} = 13.27 \text{ MPa}$ . The yield stress of the model based  
 346 on the Schmalzle slip is thus 13.28 MPa, which translates to a static friction coefficient of  
 347  $13.18/50 = 0.2656$  (Table 1). The assumed homogeneity of the yield stress can be understood as  
 348 an indication of relatively smooth megathrusts that are conducive to very large earthquakes, and  
 349 its low amplitude reflects the low fault strength as inferred from heat flow data (Gao and Wang,  
 350 2014).

351

352 The highly compliant, frontal region of the accretionary prism could significantly impact the  
 353 rupture scenarios as its inelastic deformation can act as an energy sink (Galvez et al., 2014). We  
 354 tested the sensitivity of the assumed depth limit to the weak frontal prism. We found that strong  
 355 free-surface reflections and amplified fault slip would be generated to facilitate trench-breaching  
 356 rupture if a thinner frontal prism was used, but rupture would be halted if a thicker frontal prism  
 357 was used (Figure S3). For simplicity, we adopt an average depth range (i.e. 5 – 7 km) for the  
 358 frontal prism according to the velocity model of Stephenson et al. (2017) (Figure S4). Similar to  
 359 Ramos et al. (2021), we add cohesion to the segment of the megathrust overlying the assumed  
 360 frontal prism (Figure 3c) to suppress undesired rupture initiation near the trench.

361

362 Based on seismic observations, the critical weakening distance,  $d_c$ , has been suggested to be  
 363 proportional to the local total slip, indicating spatially heterogeneous  $d_c$  on faults (Mikumo et al.,  
 364 2003; Tinti et al. 2005; Fukuyama and Mikumo, 2007). However, because the slip distribution is  
 365 now known a priori for future earthquakes, and the scaling relationship between slip and  $d_c$  has  
 366 large uncertainties (Guatteri and Spudich, 2000; Chen and Yang, 2020), there is little  
 367 information about  $d_c$ . Ensuring fair comparison among locking models is another challenge in  
 368 deciding on  $d_c$  because the same  $d_c$  represents different fracture energy given the different initial  
 369 stress and yield stress in each model. Dynamic models constructed by Weng and Yang (2018)  
 370 and Yao and Yang (2020) show that a uniform  $d_c$  yields synthetic waveforms that compare with  
 371 observations very well, and that a heterogeneous slip-scaled  $d_c$  does not lead to appreciable  
 372 improvements. Therefore, we take the simpler approach of assuming a uniform  $d_c$ . We recognize  
 373 the large uncertainties associated with the choice of  $d_c$  and test a range of uniform  $d_c$  values to see  
 374 how the results are affected. In section 4.3, we will discuss the results using  $d_c$  of 1 m and 0.6 m.  
 375

376 Our models need to meet the resolution requirement. A cohesive zone refers to the fault plane  
 377 portion behind the crack tip where shear stresses drop from static to dynamic value with a slip  
 378 less than  $d_c$  (Ida 1972). The cohesive zone of in-plane (mode II) ruptures can be estimated by the  
 379 following equation (Day et al., 2005)

$$380 \quad \Lambda = \Lambda_0 A^{-1}(v), \quad \Lambda_0 = \frac{9\pi}{32} \frac{\mu}{1-\nu} \frac{d_c}{\tau_s - \tau_d}, \quad (2)$$

381 where  $\mu$  is shear modulus,  $\nu$  is Poisson's ratio, and  $\tau_s$  and  $\tau_d$  are yield stress and dynamic shear  
 382 stress, respectively. Considering  $d_c$  of 0.6 m - 1 m, the static cohesive zone sizes are around 7.5 -  
 383 25 km. Given a lower bound for shear wave speed  $V_s$  of 3.165 km/s and a rupture speed of 3.1  
 384 km/s,  $A_{III}^{-1} = (1 - V_r^2/V_s^2)^{1/2} = 0.2$ , the dynamic cohesive size can be as small as ~1.5 km.  
 385 Aagaard et al. (2013) demonstrate that PyLith can resolve cohesive zones around 1.5 times the  
 386 size of the tetrahedral elements. Therefore, our element size of 500 m on the fault can resolve  
 387 cohesive zones in our models.

388

### 389 3.5 Rupture initiation

390

391 The nucleation zone refers to the area where the rupture begins. In the prescribed nucleation  
 392 zone, the initial stress has to meet the yield stress to initiate the rupture. To initiate a rupture,  
 393 we decrease the yield strength inside the designated nucleation zone by decreasing the static  
 394 friction coefficient within the nucleation zone from the  $\tau_s$  values shown in Table 1 to  $\tau_s^i =$

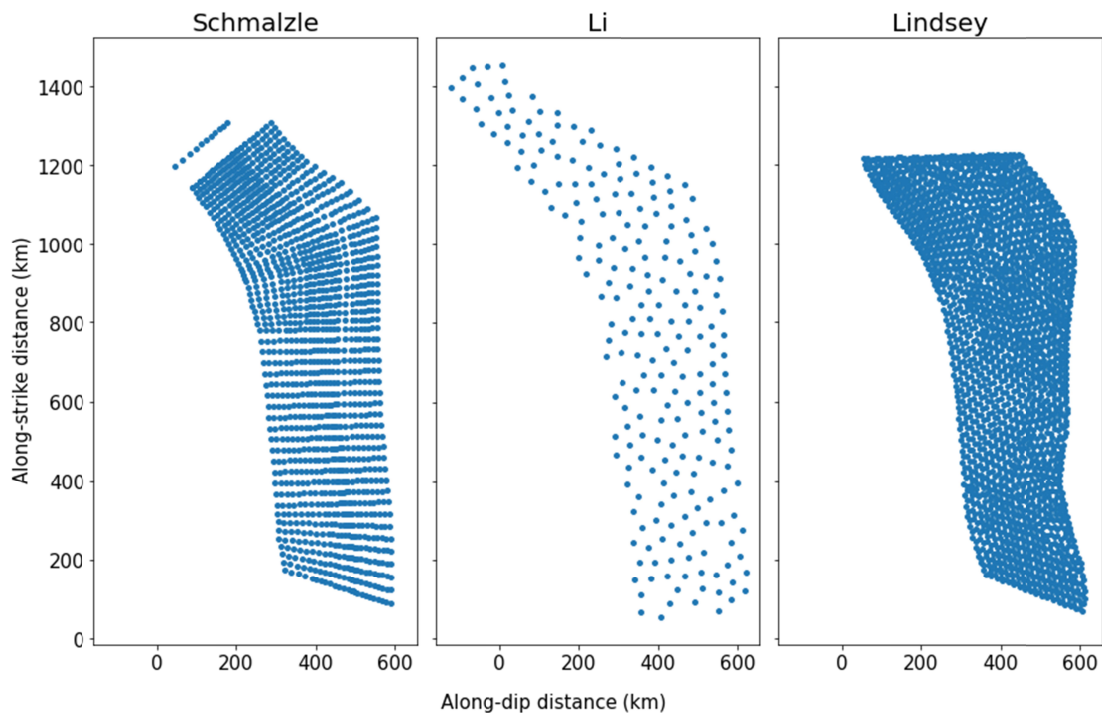
395 0.2001. In order to initiate a spontaneous rupture, a nucleation zone needs to exceed a critical  
 396 size (Yang et al., 2019a),

$$397 \quad A_1 = \frac{(3\pi)^3 \overline{\tau_0 - \tau_d} (\tau_s - \tau_d)^2}{2^{11} \tau_s - \tau_s^i (\overline{\tau_0 - \tau_d})^4} \mu^2 d_c^2 \quad (3)$$

398 So  $\overline{\tau_0 - \tau_d}$  and  $(\tau_s - \tau_s^i)$  denote average static stress drop and strength decrease within the  
 399 nucleation zone respectively. For instance, given an average static stress drop of 1.5 MPa and  $d_c$   
 400 of 0.6 m for the Schmalzle model, the critical radius of a circular nucleation zone is 13.6 km.

401  
 402 We tested nucleation zone radii of 10 km and 15 km, comparable with those adopted in  
 403 dynamic modeling studies for the 2011 M9.1 Tohoku earthquake (Duan 2012; Ide and Aochi  
 404 2012; Galvez et al. 2014). With different nucleation sizes, the model-predicted rupture  
 405 scenarios for the same hypocenter locations are similar (Figure S5). To ensure that our rupture  
 406 scenarios could represent first-order features from the interseismic locking models instead of  
 407 the interpolation methods, the nucleation zone size has to be comparable to the patch size or  
 408 node spacing used during inversion (Figure 5), especially for the Li model. Thus, we adopted a  
 409 larger radius of 15 km. We then conduct simulations on ten along-strike hypocenter locations  
 410 in southern Cascadia spanning from  $41.77^\circ - 44.47^\circ$  latitude. A range of depths is also tested  
 411 depending on the positive stress change distribution of each locking model.

412



413

414 Figure 5. Spatial distribution of original data points for the three interseismic locking models.

415

## 416 4. Results

417

### 418 4.1 Stress build-up from locking distribution

419

420 From static calculations as described in section 3.3, we obtain distributions of stress  
421 accumulation from the total slip deficit (Figure 4). Since the stress change along strike is  
422 negligibly small, only the dip component is shown in Figure 4d – 5f. Nevertheless, the strike  
423 component is used in our dynamic simulations and the points of the highest stress change are  
424 determined by the magnitude of stress change vectors. The slip deficit distributions calculated  
425 from the locking models have similar patterns and their moment magnitude within the static  
426 model domain only differs by 0.03 (i.e. Mw 8.99-9.02) (Figure 4). All of the three locking  
427 models feature high slip deficit above 12 m in northern Cascadia (above 900 km along-strike  
428 distance in Figure 4). The largest contrast between the models is in the south and central  
429 segments. For example, the segment that exhibits more creep is located at 550-750 km, 300-550  
430 km, and 500-700 km in the Schmalzle, Li, and Lindsey models, respectively, with different  
431 maximum slip deficits (Figures 5a – 5c). The derived stress accumulation distributions display a  
432 larger difference in along-strike variations among these models (Figures 5d – 5f).

433

434 The depth extent of positive stress build-up based on the Schmalzle model extends to ~20 km  
435 depth. We can locate three high-stress patches, labelled A1, A2, and A3 in Figure 4d in our  
436 dynamic model domain. A2 hosts the maximum stress build-up of 3.3 MPa. Between the A2 and  
437 A3, there is a creeping segment with obviously lower stress (labeled C in Figure 4d). Such stark  
438 along-strike variations are not that obvious in the slip deficit distribution (Figure 4a), because the  
439 stress accumulation is proportional to the second derivative of slip deficit. While A2 and A3  
440 host sharp downdip decrease in slip deficit within a narrow locking zone, the C segment has a  
441 more gradual decrease with deeper locking depths. This illustrates that the stress distributions  
442 can reveal the seismic potentials that may not be identified as first-order features in slip deficit  
443 distributions.

444

445 The stress build-up based on the Li model shows a more uniform along-strike distribution,  
446 except in the northernmost region where the highest slip deficit takes place (Figure 4). The

447 positive stress in this model extends deeper, to ~30 km depth. Although it has a longer zone of  
448 low slip deficit than in the Schmalzle model, there are no distinct high-stress patches but only a  
449 slightly low-stress patch at 400-500 km (Figure 4e). The maximum accumulated stress in the  
450 dynamic model domain is only 1.7 MPa.

451

452 The Lindsey model shows a somewhat similar along-strike variation of stress distribution to  
453 the Schmalzle model even though the amplitude is different (Figure 4). The slip deficit  
454 amplitude of the Lindsey model is significantly lower than the Schmalzle model, having  
455 maximum accumulated stress of 1.9 MPa in the north. Yet, their spatial gradient variations  
456 along strike are alike. The south and the north have steeper slip deficit gradients constrained in  
457 shallower depths ~30 km while the creeping segment has a noticeable gentle decrease in slip  
458 deficit until the slab bottom (Figure 4c). Considering that rupture segmentation is dominated  
459 by the spatial variation of stress instead of the amplitude, we expect results akin to the  
460 Schmalzle model given modifications of frictional parameters regarding the amplitude.  
461 Because of the poorly constrained down-dip locking depths, the Lindsey stress model is not  
462 further evaluated for dynamic simulations.

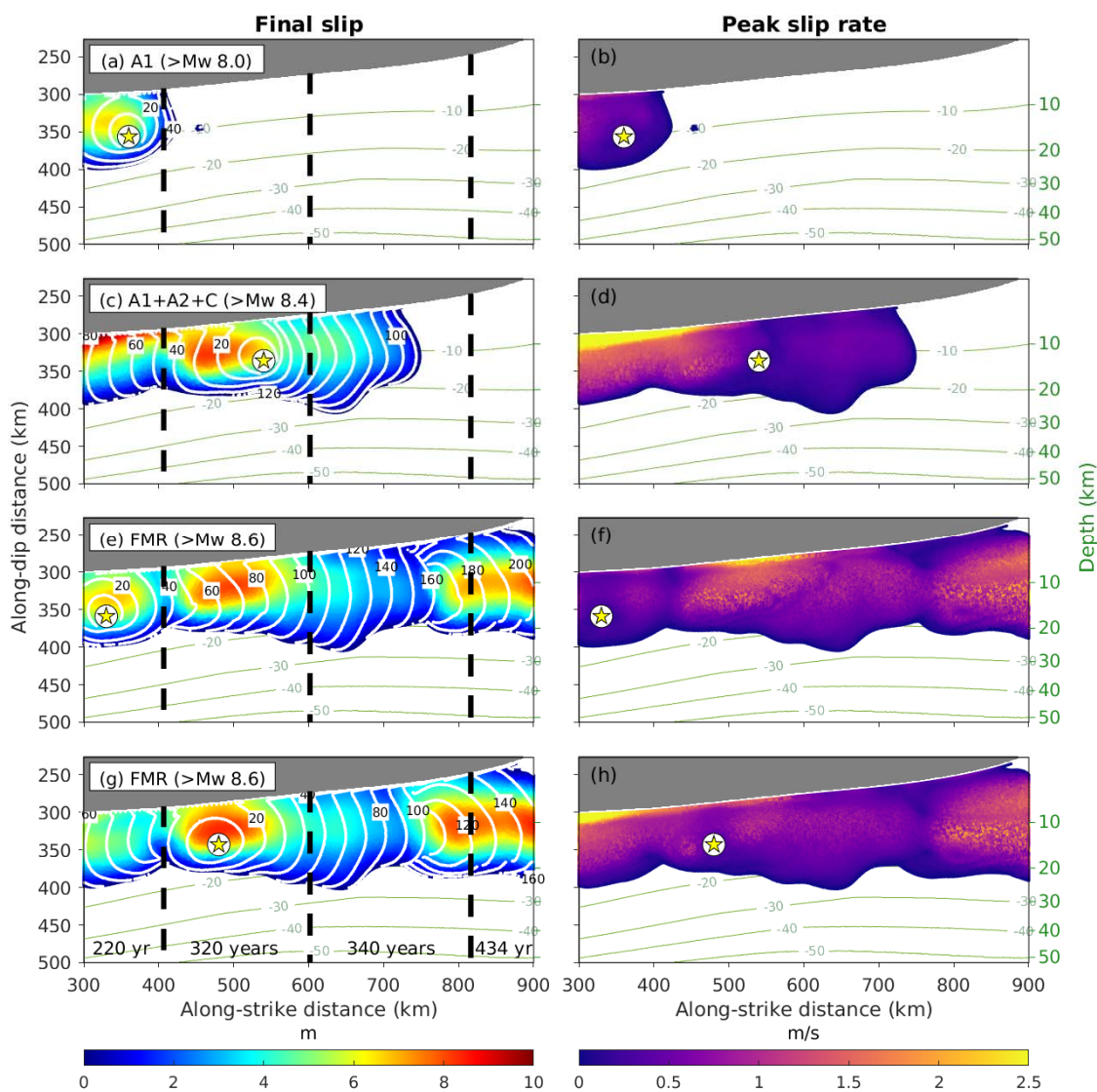
463

#### 464 4.2 Predicted rupture scenarios

465

466 Using the initial stress which includes accumulated stress derived from locking models, we  
467 initiate the ruptures with a range of hypocenter locations. In some dynamic scenarios, the  
468 ruptures propagate outside with considerable rupture extent, classified as breakaway scenarios.  
469 The examples of breakaway scenarios using  $d_c$  of 0.6 m and 1 m are shown in Figure 6-7 and  
470 Figure S6 respectively. While in other cases, the rupture propagation stops immediately outside  
471 the nucleation zones due to the lack of elastic energy release to overcome the fracture energy  
472 required to weaken the fault, termed self-arresting events (Figure 8). The moment magnitude  
473 for scenarios is calculated according to the integral of the final slip ( $d$ ) over the fault plane area  
474 ( $A$ ) using an average shear modulus ( $\mu$ ) of 35 GPa ( $M_0 = \mu A d$ ;  $M_w = 2/3 * (\log_{10}(M_0) - 9.1)$ ). Our  
475 moment magnitude gives a lower limit for the scenarios that propagate out of the model  
476 domain (e.g. Figure 6e & 6g). The slip rate means the relative particle velocity across the fault  
477 while the rupture speed is the rate of rupture front movement (Rowe and Griffith, 2015),  
478 calculated every 10 seconds.

479

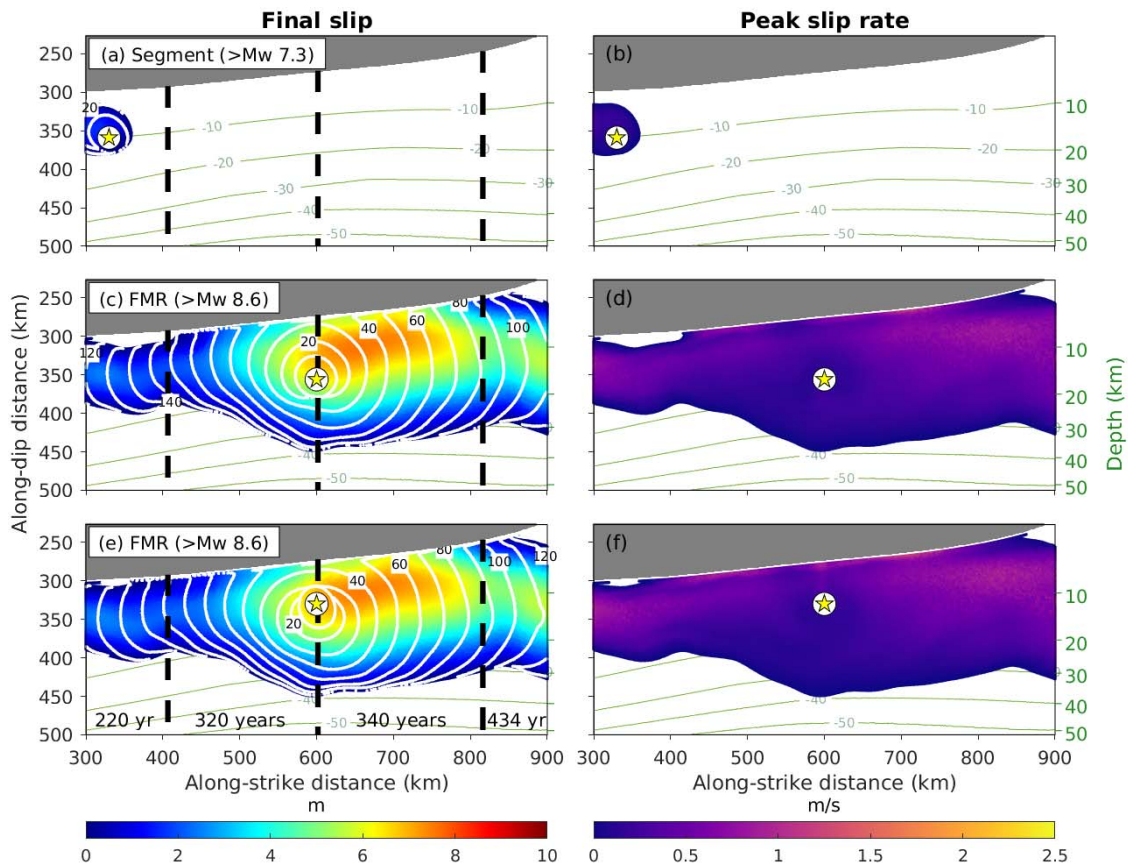


480

481 Figure 6. Dynamic rupture scenarios derived from the stress distribution of the Schmalzle  
 482 model using a  $dc$  of 0.6 m. (a), (c), (e), (g): Final slip distribution. Stars: hypocenter locations.  
 483 Olive-green contours: slab depth contours. Rupture fronts (white contours) are displayed every  
 484 10 seconds and numbered every 20 seconds. Black dashed lines: recurrence time intervals of  
 485 220, 320, 340, and 434 years (Goldfinger et al., 2017) as written in (g). The labeled Mw is  
 486 calculated by slip within the model domain, thus scenarios with slip extending outside the  
 487 domain should have larger magnitudes. (b), (d), (f), (h): Peak slip rate throughout the rupture.  
 488 Stars: hypocenter locations. Olive-green contours: slab depth contours. (a) – (b): Scenario  
 489 rupturing the A1 asperity. (c) – (d): Scenario rupturing A1 and A2 asperities and part of the  
 490 creeping segment C. (e) – (f): Full-margin rupture (FMR) initiated from A1. (g) – (h):  
 491 Full-margin rupture initiated from A2.

492

493



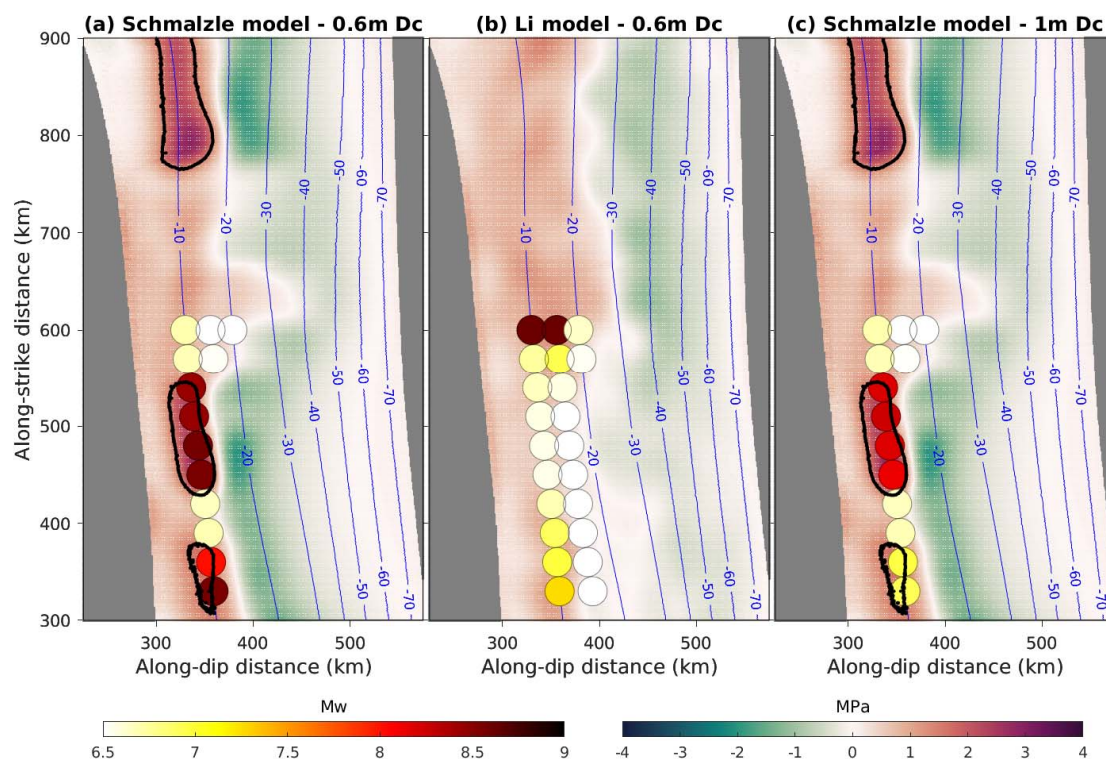
494

495 Figure 7. Dynamic rupture scenarios derived from the stress distribution of the Li model using  
 496 a dc of 0.6 m. Same as Figure 6, except for the Li model. (a) – (b): Segmented rupture scenario.  
 497 (c) – (f): FMR for different hypocenter locations.

498

499 We further classify the self-arresting and breakaway events explicitly. According to the  
 500 empirical relationships between the rupture area and magnitude, the rupture within the  
 501 nucleation zone is around Mw 6.5 (Wells and Coppersmith, 1994). Earthquakes generally have  
 502 rupture velocities higher than 1 km/s (Rowe and Griffith, 2015) and demonstrate a ratio  
 503 between rupture velocity and  $v_s$  starting from around 0.4 (Weng and Ampuero, 2020). Since  
 504 our  $v_s$  at trench (5 km depth) is 3.17 km/s, we expect breakaway ruptures to reach rupture  
 505 velocities higher than 1.27 km/s ( $0.4 v_s$ ). Consequently, we define the scenarios with Mw < 6.5  
 506 and rupture speed less than 1.27 km/s as self-arresting ruptures, and those above as breakaway  
 507 ruptures. Our analysis will only focus on the breakaway ruptures, considering self-arresting  
 508 ruptures are merely the results of artificial nucleation.

509



510

511 Figure 8. Moment magnitude dependence on hypocenter locations. Map view of the moment  
 512 magnitudes of rupture scenarios nucleated at each location (circles) with the stress build-up in  
 513 the background, and slab depth contours (blue lines). (a) Scenarios derived from the Schmalzle  
 514 model using a dc of 0.6 m. Black lines: 1.5 MPa stress contour, same as in Figure 4. (b)  
 515 Scenarios acquired from the Li model using a dc of 0.6 m. (c) Same as (a) except for a dc of 1  
 516 m (Figure S6).

517

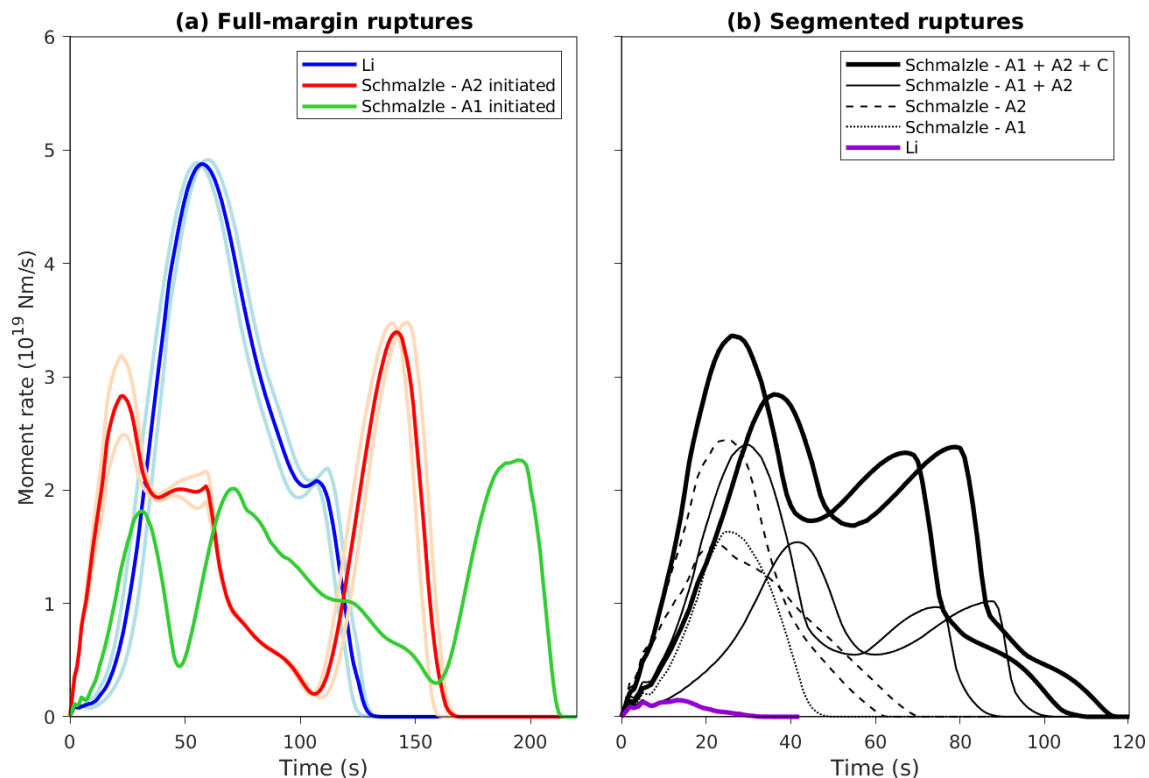
518 We further divide the breakaway ruptures into segmented ruptures and full-margin ruptures.  
 519 “Full-margin ruptures” represent rupture scenarios that propagate out of the entire model  
 520 domain. Because the northern Cascadia holds the highest accumulated stress and our model  
 521 domain includes a part of the northern segment, it is reasonable to assume that the ruptures  
 522 propagating out of the domain’s northern boundary would eventually rupture the entire  
 523 northern Cascadia. Similarly, the southern segment inside the domain has consistent stress  
 524 levels with the southernmost Cascadia outside of the domain, hence we assume the  
 525 “full-margin ruptures” can break the southern Cascadia as well. For this reason, we name the  
 526 ruptures propagating out of the south and north of the domain as “full-margin ruptures” in the

527 following context. In contrast, the scenarios where their along-strike rupture extents within the  
 528 model domain are regarded as segmented ruptures.

529

530 Full-margin ruptures are shown in both the Schmalzle-based (Figure 6e-h) and the Li-based  
 531 scenarios (Figure 7c-f) with maximum final slips of 8.5 m and 7.6 m respectively. Those of the  
 532 Schmalzle model are larger than Mw 8.6, reaching a rupture speed of 3.1 km/s and a peak slip  
 533 rate of 4.5 m/s. The source durations last for more than 150-200 seconds depending on the  
 534 hypocentre location (Figure 9a). On the other hand, the moment magnitudes of full margin  
 535 ruptures from the Li model are also higher than Mw 8.6. They have a slightly lower rupture  
 536 velocity of 2.7 km/s and a peak slip rate of 1.4 m/s. The source duration is less than 140  
 537 seconds (Figure 9a). The full-margin ruptures of the Schmalzle model and the Li model halted at  
 538 30 km and 40 km depths respectively. All are initially predominated by crack-like ruptures,  
 539 evolving into pulse-like ruptures (Movies S1-S4).

540



541

542 Figure 9. Moment rate functions from dynamic rupture simulations. (a) Moment rate of all  
 543 full-margin rupture scenarios. Moment rate functions of individual neighboring rupture  
 544 scenarios are indicated by lighter colors (light blue for the Li model and pink for those initiated  
 545 from A2 in the Schmalzle model) and the average is marked by solid colors (blue for the Li

546 model and red for the A2 initiation in the Schmalzle model). Note that there is only one event  
547 initiated from A2 in the Schmalzle model (green line). (b) Moment rate of all segmented  
548 ruptures for the Schmalzle model (black lines) and Li model (purple line). A1 and A1+A2+C  
549 ruptures were derived using a dc of 0.6 m while A2 and A1+A2 scenarios were simulated with  
550 a dc of 1 m (Figure S6). The only segmented event from the Li model utilizes a dc of 0.6 m.

551

552 Despite having the same accretionary wedge setting as in Figure S4b, all the scenarios shown  
553 here, except case 6c, do not demonstrate the large near-trench slip as tested above because of the  
554 different hypocenter locations and stress distribution. For the Schmalzle model, as the rupture  
555 initiates in the south, the combined effects from rupture directivity and free surface reflection in  
556 the south are smaller as compared to initiation from the north. As for the case of 6c, its  
557 hypocenter is located further north, thus allowing a stronger directivity. However, such high slip  
558 trench features are also absent in the north even with hypocenters in the south. This is because  
559 while the rupture propagates through the central creeping segment, the energy depletes and it is  
560 insufficient to cause a large slip until it reaches the high-stress asperity at the north. For the Li  
561 model, the high-slip trench is also absent because there are no particular high-stress asperities  
562 that could trigger larger slip near the trench.

563

564 Rupture segmentation is observed in both models. From the Schmalzle model dynamic  
565 scenarios, we observed one scenario breaking A1 (Figure 6a) and two scenarios rupturing A1,  
566 A2, and partly C (Figure 6c). The A1 segmented rupture (Figure 6a) is initiated by a hypocenter  
567 location at A1 asperity and the source duration continues for 40 seconds (Figure 9b), with  
568 rupture stopped above 20 km depth. Both A1+A2+C scenarios (Figure 6c) are triggered by  
569 nucleation at A2 asperity, and the source durations last for 110-120 seconds (Figure 9b), having  
570 slip above 30 km depth. For the Li model, only one dynamic segmented scenario is found  
571 rupturing the southernmost segment. Since the rupture initiation is close to the domain boundary,  
572 the rupture propagates out of the south quickly after nucleation while being arrested in the north  
573 and above 20 km depth (Figure 7a), resulting in a duration time as short as 30 seconds (Figure  
574 9b). Except for the A1+A2+C dynamic models which have similar rupture evolution behaviors  
575 to the full-margin ruptures (Movie S5), the short segment ruptures (Figure 6a and 7a) are  
576 primarily crack-like ruptures as the rupture duration is insufficient for them to grow into pulses  
577 (Movies S6-7).

578

## 579 4.3 Hypocentral effects on the potential moment magnitude and ground surface response

580

581 In view of the different resulting scenarios, we investigate the effect of different hypocenters in  
582 both models with a  $d_c$  of 0.6 m. For the heterogeneous Schmalzle model, there is a strong  
583 along-strike variation in moment magnitude with respect to the stress distribution (Figure 8a).  
584 The nucleation zones within the highest stress patch A2 result in scenarios with  $M_w > 8.4$ -8.6  
585 and the events within A1 have  $M_w > 8.0$ -8.6. All the nucleation centers lying outside of the stress  
586 asperity results in self-arresting ruptures. This demonstrates the hypocentral dependency of  
587 magnitudes in the Schmalzle model.

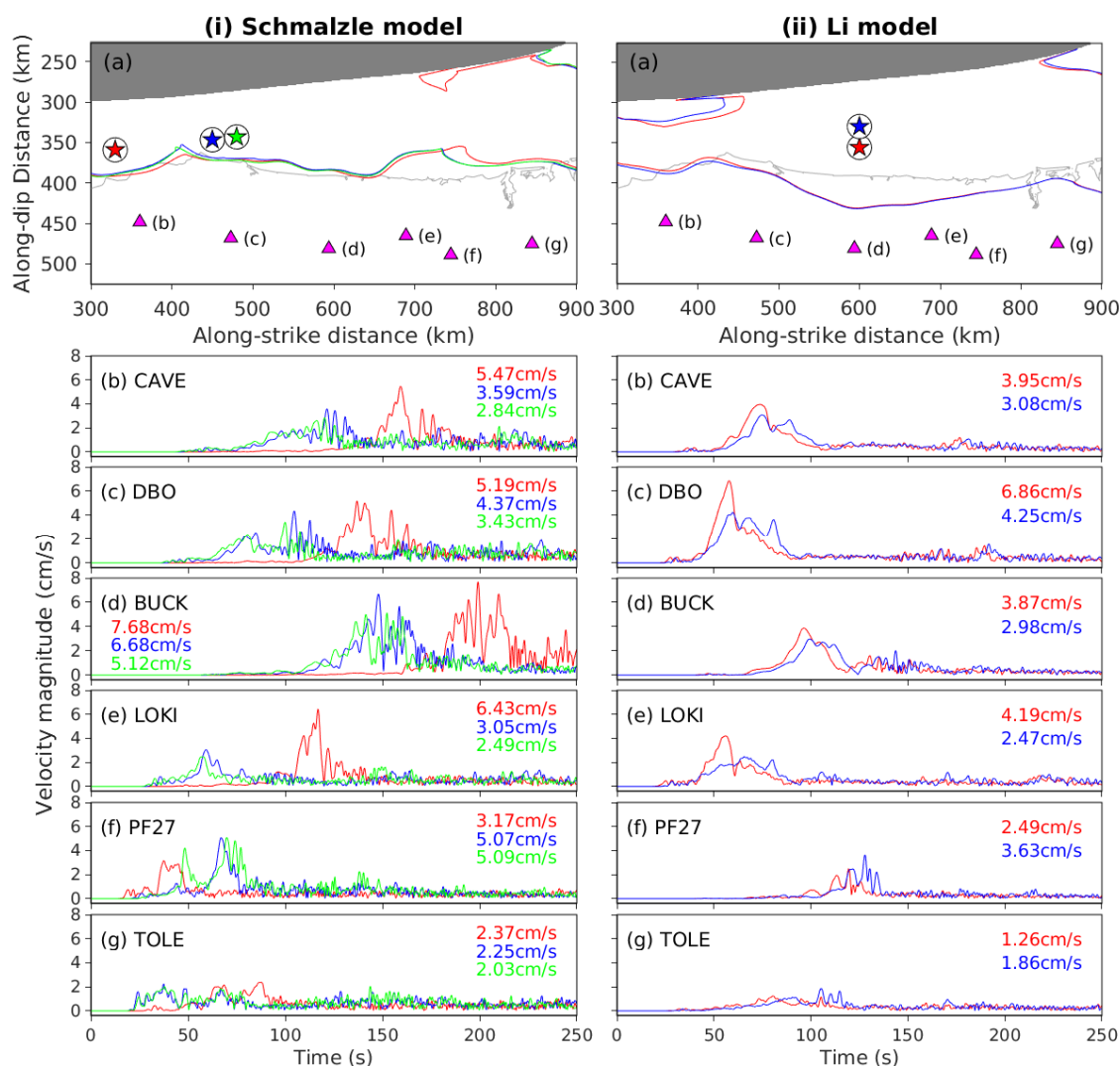
588

589 Meanwhile, the Li geodetic locking model gives a smoother and more homogeneous stress  
590 distribution within the model domain that does not favor rupture segmentation except in the  
591 southernmost region where the initial stress is slightly higher (Figure 8b). Although full-margin  
592 ruptures take place with hypocenters in a particular region, it by no means suggests that the  
593 ruptures are larger on that site. It shows that the initiation of full-margin ruptures is sensitive to  
594 slight stress perturbations on the fault. Recalling our assumptions of linear stress accumulation  
595 and uniform background stress level, small deviations on these assumptions (e.g., spatial  
596 variations in stress accumulation time and material properties) could cause comparable stress  
597 distribution perturbations in the Li model while the perturbations would be relatively  
598 insignificant in the Schmalzle model. Thus, the Schmalzle model shows clearer seismic  
599 potential while the Li model is more ambiguous considering the uncertainties in stress  
600 accumulation evolution and background stress field.

601

602 Apart from the moment magnitude, the hypocentral effects on ground surface response are also  
603 noticeable. We compare the velocity magnitude of synthetic stations near major cities derived  
604 from the margin-wide scenarios in both models (Figure 10). Although the rupture extent from  
605 the scenarios of different hypocentres in each model is highly similar (Figure 10a), the  
606 amplitude of peak ground velocity can differ twice. For instance, in the Li model, the two  
607 hypocenters have the same along-strike distance but different downdip depths - 10 km and 15 km.  
608 The deeper nucleation event (15 km) clearly demonstrates larger peak ground velocities than the  
609 shallower one (10 km) at stations CAVE, DBO, BUCK, and LOKI. Such a difference is  
610 primarily due to the rupture propagation. For the 15 km event, the rupture propagates updip since  
611 initiation, setting off a strong wavefront (Figure 7c). However, the 10 km event starts by

612 propagating downdip and is followed by updip fault slip along the sides of the nucleation zone,  
 613 creating two wavefronts shortly after the nucleation (Figure 7e). The interference of these  
 614 seismic waves and those from downdip fault slip leads to a more ambiguous waveform slightly  
 615 lagging behind the 15 km event even though the 10 km one is in closer proximity to the surface.  
 616



617  
 618 Figure 10. Synthetic velocity magnitude at stations for FMR. (a) The 1 m final slip contour of  
 619 rupture scenarios with the coastline (light grey). The colors of the slip contours match with the  
 620 star (hypocenter location) colors. Magenta triangles: station locations. Labels beside stations:  
 621 the plot number. The stations near major cities along the strike are selected from the Pacific  
 622 Northwest Seismic Network. (b) – (g) Comparison of velocity magnitudes (three-component  
 623 combined) among the rupture scenarios in (a) with matching colors. The corresponding peak  
 624 velocity magnitudes and station names are marked on each trace. (i) Schmalzle model. (ii) Li  
 625 model.

626

627 The hypocentre at a different location along-strike also results in different waveforms. In the  
628 Schmalzle model, there are two hypocentres in A2 and one hypocentre in A1 contributing to  
629 margin-wide ruptures. Since the A1 hypocentre event propagates from the southernmost region  
630 to the north of the domain, the strong directivity causes a distinct pulse as compared to the A2  
631 hypocentre events. For example, the LOKI station has peak velocity magnitudes of 2.5-3 cm/s  
632 for the A2 hypocentres but 6.4 cm/s for the A1 hypocentre (Figure 10ei).

633

#### 634 4.4 Seafloor deformation and coastal subsidence in margin-wide scenarios

635

636 We also evaluate the surface deformation patterns for our margin-wide rupture scenarios. The  
637 peak vertical ground displacements for the Schmalzle-based and Li-based scenarios are similar  
638 in magnitude, ranging from -1.1 m to +1.0 m and from -1.2 m to +1.1 m respectively. On the  
639 other hand, the maximum peak ground velocity of the Schmalzle-based scenarios (i.e. 2.3 m/s)  
640 is remarkably higher than that of the Li-based scenarios (i.e. 1.2 m/s) by almost double. Both  
641 models show the highest peak ground velocity towards the tip of the continental crust and the  
642 northernmost region of the domain.

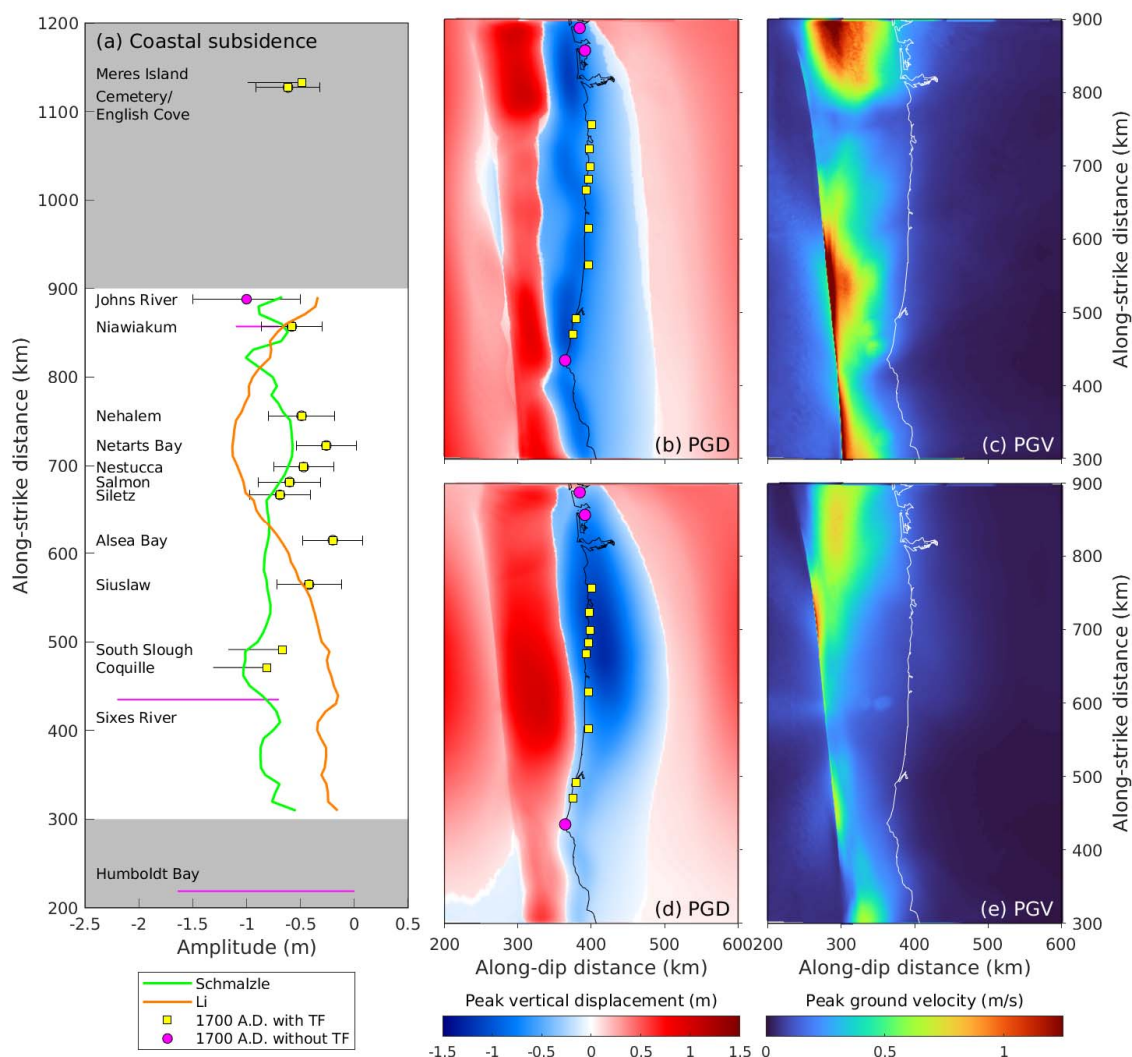
643

644 Coseismic hingeline refers to the point where there is zero seafloor vertical displacement.  
645 Compared to the Schmalzle model (Figure 11b), the coseismic hingeline for the Li model  
646 (Figure 11d) is further inland, especially for the central and northern segments because the  
647 down-dip rupture extent of these regions in the Li's model is deeper (Ramos et al., 2021).  
648 However, it is noted that the down-dip locking depth of the seismogenic zone is poorly  
649 constrained by geodetic data (Wang and Tréhu, 2016), thus we only focus on the along-strike  
650 variations of coastal subsidence instead of the absolute amplitudes.

651

652 The average coastal subsidence is then extracted from the peak vertical ground displacement of  
653 the data points closest to the coastline in all the margin-wide scenarios in both models (Figure  
654 11a). We then compare the synthetics with the subsidence records of the A.D. 1700 M9  
655 earthquake. In our scenarios, Li's coastal subsidence gives a more distinct pattern compared to  
656 the observations, having the largest amount of deformation at the high slip patch in the north and  
657 decreasing further away. For scenarios from Schmalzle model, the along-strike coseismic  
658 subsidence appears to fluctuate with slightly larger deformation in high-slip segments region.

659 The subsidence records of the A.D.1700 M9 rupture also exhibit heterogeneous along-strike  
 660 pattern, which can be matched by models with several high slip patches (Wang et al., 2013). In  
 661 our case, the scenarios from Schmalzle model can reproduce a similar along-strike variation  
 662 with the observations, mainly due to the higher slip heterogeneity with three high-slip patches  
 663 (Figure 6) compared to those from Li model (Figure 7).  
 664



665  
 666 Figure 11. Ground motion intensities of full-margin ruptures. (a) Average peak vertical ground  
 667 displacement along the coastline for the Schmalzle model (green line) and the Li model  
 668 (orange line). Yellow squares: observations sites with transfer function analysis (TF). Pink  
 669 circles: sites without TF. Error bars: one standard deviation. Black lines with yellow squares at  
 670 one end: yellow squares as the minimum estimates. Pink line: uniform distribution. Grey  
 671 patches: regions outside of the model domain. (b) Peak vertical ground displacement of  
 672 full-margin ruptures in Schmalzle model with the coastline (black line). Observation sites with

673 (yellow square) and without (pink circles) TF analysis (Wang et al., 2013). (c) Average peak  
674 ground velocity PGV of FMR derived in the Schmalzle model with the coastline (white line).  
675 (d) – (e): Same as (b) and (c) respectively except for the Li model.

676

## 677 5. Discussions

678

### 679 5.1 Potential rupture patterns in correlation with recorded segmentation and recurrence 680 intervals

681

682 The rupture extents of segmented scenarios in the Schmalzle model are consistent with the  
683 recorded segmentation of paleoearthquakes (Goldfinger, 2012, 2017). The A1 scenario arrested  
684 around the 220-320 years recurrence interval boundary (Figure 6a), and all cases for A2 and  
685 A1+A2 ruptures stopped around the 320-340 years boundary as it enters the creeping segment  
686 (Figure S6). For A1+A2+C cases, the ruptures extend to part of the 340-year recurrence interval  
687 segment but not the whole (Figure 6c). This is because the A3 asperity is located slightly off the  
688 recurrence interval boundary. Therefore, the ruptures could either arrest before A3 or propagates  
689 to the rest of the high-stress northern region, causing full-margin ruptures. There are also  
690 ambiguities in determining the paleoseismic rupture limits due to limitations in core data. Hence,  
691 the A1+A2+C scenario is supported by the estimated minimum rupture limit in the segmented  
692 rupture model (Goldfinger et al., 2017) where rupture stops before the 340-year segment. On the  
693 other hand, the Li model does not share particular similarities with the recurrence interval  
694 segments within the model domain.

695

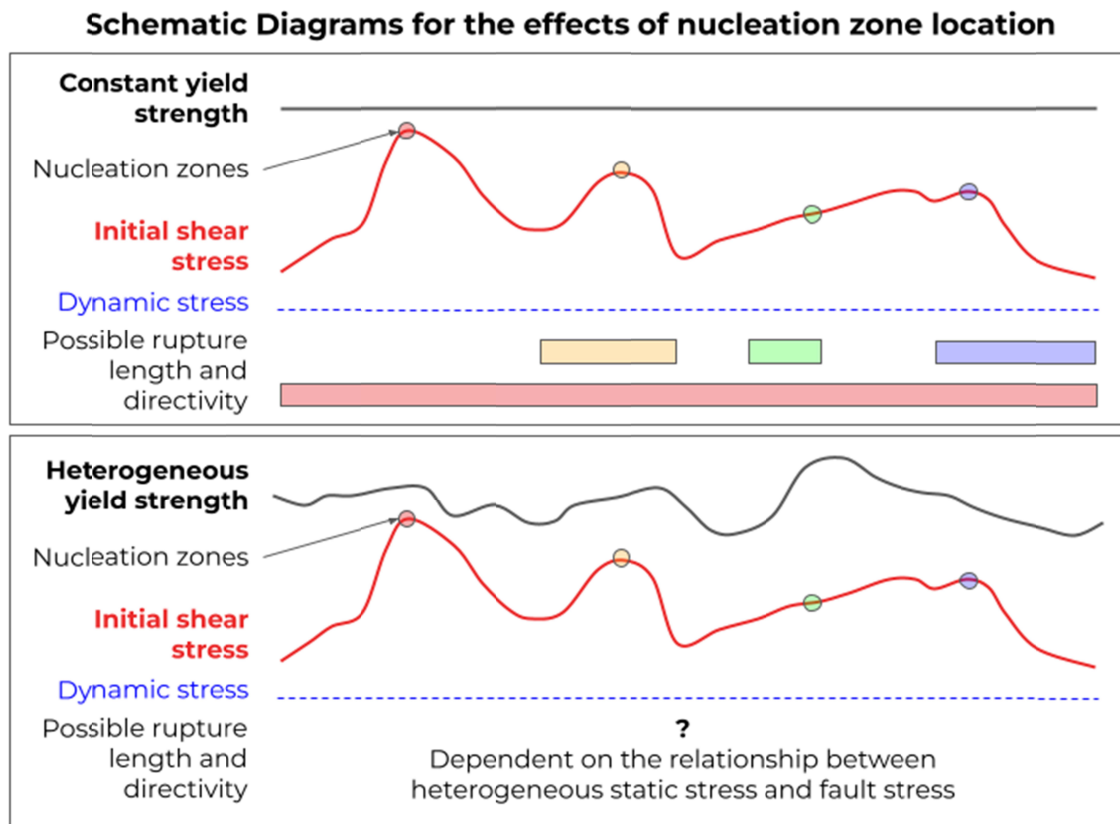
696 We also find that the margin-wide ruptures can be derived for all models given certain  
697 frictional parameters. Given the 320 years of silence and the recurrence intervals of 220-340  
698 years in the south, all segmented scenarios are possible in the current stage. Although there are  
699 few constraints on the frictional parameters of the Cascadia megathrust, our combination of  
700 parameters allows variations in rupture scenarios, including segmented and margin-wide  
701 ruptures comparable with the geological records. This may suggest that the ratio between the  
702 frictional parameters and initial stresses is reasonable, if not the absolute amplitudes. The  
703 margin-wide rupture initiates at A1 and A2 in the Schmalzle model and the boundary between  
704 320 and 340 recurrence intervals for the Li model. This reflects that at the current state, the

705 possibility of ruptures initiating from the south or central Cascadia growing into a margin-wide  
 706 rupture cannot be eliminated.

707

708 The diverse segmentation in our scenarios results from heterogeneous locking and various  
 709 hypocentre locations. Ramos et al. (2021) initiated dynamic rupture simulations at locations of  
 710 highest stress drop in the south, resulting in full-margin ruptures for scenarios with uniform  
 711 stress accumulation time, and both full-margin and segmented rupture scenarios using  
 712 heterogeneous stress accumulation time along strike which is determined empirically. Indeed,  
 713 the uncertainties in the stress accumulation history could be introduced by a heterogeneous  
 714 time interval. However, with strong along-strike differences in accumulation time, the stress  
 715 distribution becomes largely affected by the empirical time interval instead of the locking  
 716 distribution. Our study shows that segmented ruptures are possible even using a uniform stress  
 717 accumulation time when different nucleation zones are used. The application of hypocentre  
 718 locations discovers the possibilities of rupture initiation from a range of stress drops, thus more  
 719 segmentation patterns are found apart from the largest possible margin-wide ruptures (Figure  
 720 12).

721



722

723 Figure 12. A schematic diagram demonstrating the potential rupture segmentation by applying  
724 different hypocenter locations.

725

726 5.2 Simulated coseismic subsidence compared with A.D. 1700 records

727

728 Although the along-strike variation of the heterogeneous Schmalzle-based coastal subsidence  
729 has a reasonable consistency with the paleoseismic records, our synthetic subsidence is  
730 generally slightly larger than the observations, exceeding one standard deviation in two sites  
731 (i.e., Alsea Bay and Siuslaw) at the central segment. Here we will provide possible reasons for  
732 such discrepancy.

733

734 Similar to the earthquake sequence simulations (Li and Liu, 2021), our subsidence is larger  
735 than the observational data at Alsea Bay. Our research focuses on estimating future  
736 earthquakes thus we assume homogenous background stress levels immediately after the A.D.  
737 1700 margin-wide rupture. However, the background for A.D. 1700 could in fact be  
738 heterogeneous due to the spatial and temporal uncertainties in the geodetic locking and the slip  
739 history before the A.D. 1700 rupture. It is possible to reconstruct best-fit subsidence results by  
740 adjusting accumulation time empirically as in Ramos et al. (2021) but this is beyond the scope  
741 of our study.

742

743 Another important factor controlling subsidence is the inelastic accretionary prism deformation.  
744 One outstanding example is the 2011 Tohoku-Oki earthquake where the region of the largest  
745 slip does not cause the largest tsunami height possibly due to the inelastic deformation of the  
746 accretionary prism (Fujiwara et al. 2017; Wilson and Ma, 2021). Han et al. (2017) observed an  
747 along-strike variation for the consolidation state of the accreted sediments in Cascadia and  
748 propose that this could contribute to the megathrust slip behavior. For instance, offshore  
749 Washington has over-consolidated sediments incorporated into the mechanically strong outer  
750 wedge, and very little sediment is being subducted, favoring potential near-trench rupture. On  
751 the other hand, a thick sequence of under-consolidated fluid-rich sediment is subducting  
752 offshore Central Oregon, possibly facilitating elevated pore pressure, thus promoting possible  
753 aseismic slip in this area. These factors may account for the slight deviation of our model  
754 subsidence from the data.

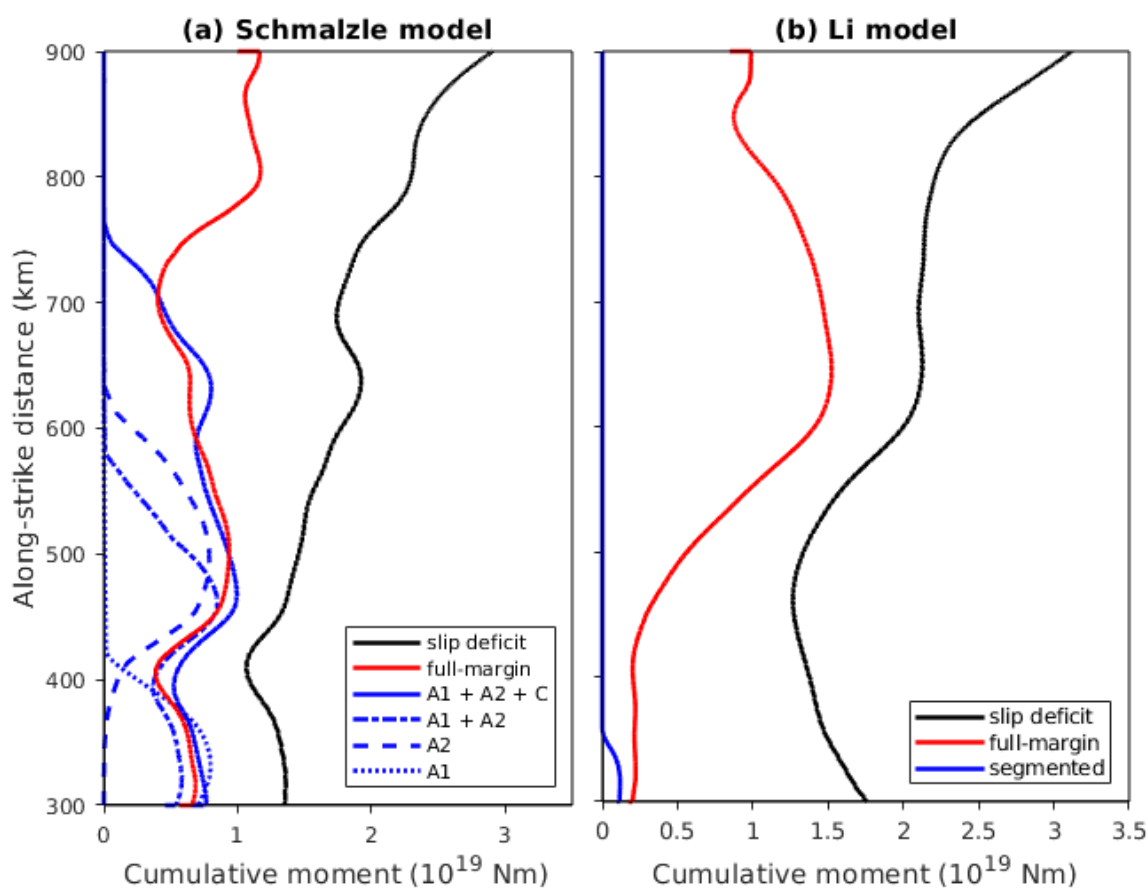
755

## 756 5.3 Comparison between dynamic simulations and static methods

757

758 Our dynamic simulation showcases a lower moment release in all rupture scenarios than  
 759 estimations from variant static methods. Static methods commonly provide the upper bound of  
 760 possible slip by assuming complete release of slip deficit in future earthquakes (Figure 13).  
 761 The maximum slip deficits within the model domain for both models only differ slightly – 12.9  
 762 m for the Schmalzle model and 13.0 m for the Li model. Consequently, the maximum slip in  
 763 the Schmalzle-based dynamic rupture model (8.5 m) contributes about 66% of the maximum  
 764 slip deficit, and that of the Li model (7.6 m) is about 59%. This difference with the static  
 765 locking models is observed in a number of studies, including the potential rupture  
 766 segmentations for the Anninghe fault in west China (Yao and Yang, 2022), the central  
 767 American subduction zone where the 2012 Nicoya Mw 7.6 earthquake occurred (Yang et al.,  
 768 2019a), Himalaya front where the 2015 Nepal Mw 7.8 earthquake took place (Li et al., 2016),  
 769 as well as the south American subduction zone where the 2010 Maule Mw 8.8 earthquake  
 770 occurred (Moreno et al., 2010).

771



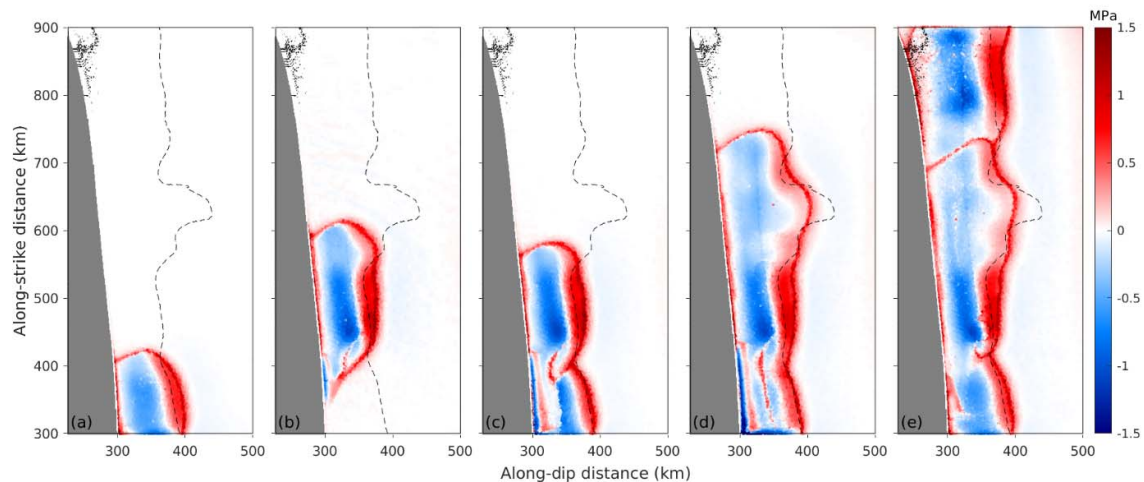
772

773 Figure 13. Cumulative moment versus the along-strike distance. The cumulative moment is the  
 774 product of rigidity, slip, and area, integrated over every 500m width along strike. Blue lines:  
 775 average cumulative moment for the segmented scenarios. Red lines: average cumulative  
 776 moment for full-margin ruptures. Black lines: cumulative moment assuming all slip deficit in  
 777 Figure 4 are released, also known as the moment deficit (Maurer et al. 2017). (a) Dominant  
 778 dynamic rupture scenario types and slip deficit for the Schmalzle model. (b) Same as (a) except  
 779 for the Li model.

780

781 These suggest that given our current frictional parameters, a considerable fraction of the slip  
 782 deficit in regions of low to moderate stress drop is not released during dynamic simulations in  
 783 our models (Figure 14 and 15). The stresses on these areas can be relieved later possibly in  
 784 form of coseismic events and slow slip events. For instance, Cascadia is well-known for its  
 785 episodic tremor and slow slip events. In addition, considering the poorly constrained downdip  
 786 limit of the seismogenic zone using geodetic observations, the unreleased slip deficit may in  
 787 fact represent uncertainties, including the portion for interseismic stress relaxation and the  
 788 temporal variation in locking width (Wang and Tréhu, 2016). Therefore, the discrepancy  
 789 highlights the necessity of conducting dynamic simulations on top of static calculations.

790

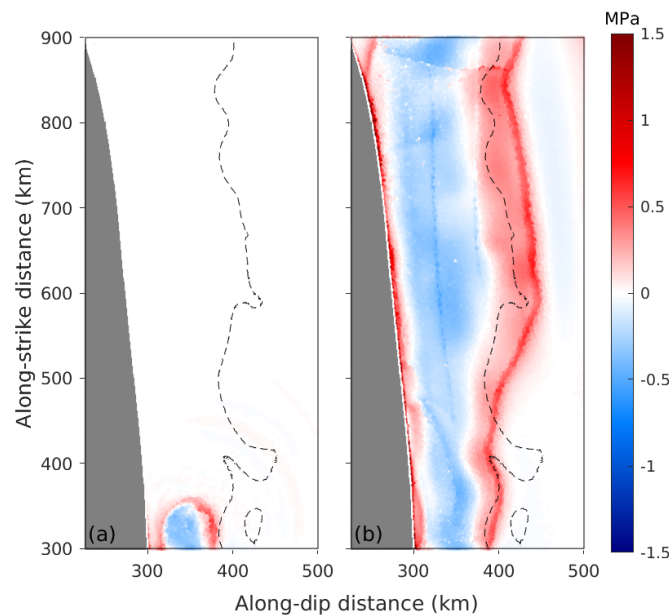


791

792 Figure 14. Stress change distributions for the Schmalzle -based rupture scenarios. Dashed lines:  
 793 contours of zero stress change derived from locking models (Figure 4). The up-dip portion of  
 794 the contour contains positive stress build-up. (a) Example of A1 rupture (Figure 6a). (b)  
 795 Example of A2 rupture (Figure S6c). (c) Example of A1+A2 rupture (Figure S6e). (d) Example  
 796 of A1+A2+C rupture (Figure 6c). (e) Example of a full-margin rupture (Figure 6g).

797

798 We further compared our results with the heterogeneous ruptures inferred from coastal  
 799 subsidence estimates. Wang et al. (2013) proposed a range of heterogeneous slip models for the  
 800 A.D. 1700 event using a 3D elastic dislocation model with reference to the subsidence  
 801 estimates. Assuming the fault slip patches follow the bell-shaped function, they adjusted the  
 802 slip patches parameters (e.g., size, location, and peak slip) to match the model-predicted  
 803 surface deformation to the paleoseismic subsidence estimates using a trial-and-error approach.  
 804 In particular, they preferred a model consisting of four high-slip patches for simplicity and  
 805 having a reasonable fit with the observations. However, the models are limited by the large  
 806 subsidence data gaps in northern and southern Cascadia (Figure 11).  
 807



808  
 809 Figure 15. Stress change distributions for the Li-based rupture scenarios. (a) Example of  
 810 segmented rupture (Figure 7a). (b) Example of a full-margin rupture (Figure 7e).

811

812 In comparison, our scenarios incorporate the locking models utilizing Global Navigation  
 813 Satellite System GNSS data, which are more densely spaced along Cascadia, as the physical  
 814 constraints on rupture depth and heterogeneities. We demonstrate that three high-slip patches  
 815 in a dynamic rupture model could be sufficient to generate subsidence amplitudes similar to the  
 816 observation of the A.D. 1700 megathrust earthquake. Similarly, the Schmalzle  
 817 locking-constrained earthquake sequence simulation (Li and Liu, 2021) also suggests a three  
 818 high-slip patches scenario, and its synthetic subsidence is in good agreement with the

819 observational data. Therefore, the three high-slip patches scenarios could be close to the  
820 A.D.1700 event.

821

#### 822 5.4 Limitations in deriving future coseismic slip

823

824 Although our dynamic models produce reasonable ground motions that match with multiple  
825 observational studies, there are limitations in constraining the up-dip frictional properties and  
826 rupture behaviors. The first concern comes from the frictional behaviors of the frontal prism. In  
827 our model, the strength drop (difference between static and dynamic stress) at the frontal prism  
828 decreases towards the trench, and the initial stress equals the addition of dynamic stress and  
829 stress drop from static simulation. Although cohesion could suppress fault failure at the  
830 beginning of the simulations, the stress perturbations from ruptures could induce higher slip  
831 rates at shallow depths as it easily overcomes the small strength drop, especially with the  
832 dynamic effects of free-surface reflection. However, in reality, velocity-strengthening materials  
833 are known to slip at low rates. Our models do not consider the plastic deformation of the  
834 frontal prism either. Indeed, cohesion could partly describe the energy absorption close to the  
835 free surface caused by the presence of unconsolidated gouge and clays (Galvez et al., 2014).  
836 However, the amplitude of cohesion in our case is not constrained by laboratory experiments,  
837 including local mineralogy, lithology, and fluid pressure. Moreover, the frictional behaviors in  
838 our model are prescribed for the fault interface and off-fault plasticity is neglected. Ulrich et al.  
839 (2022) and Wilson and Ma (2021) highlight the inelastic deformation of sediments as one of  
840 the dominant factors controlling seafloor deformation, hence tsunamic genesis. Incorporating  
841 off-fault plasticity and careful descriptions of frictional behaviors with respect to laboratory  
842 experiments and offshore geological studies would help establish realistic dynamic rupture  
843 scenarios.

844

845 Another major concern in estimating tsunami hazards comes from the uncertainty in future  
846 shallow rupture behavior. In our model, we assumed a simplified fault geometry where the  
847 fault extends to the top of the model domain, introducing trench-breaching ruptures in our  
848 dynamic models. Nevertheless, other rupture modes such as buried rupture, splay-faulting, and  
849 activation of thrusts and back-thrusts are possible (Wang and Tréhu, 2016). Gao et al. (2018)  
850 constructed hypothetical splay-fault geometries in addition to Priest et al. (2009) and a  
851 continuous along-strike frontal thrust model based on seismic profiles. Therefore, a more

852 detailed 3D mapping of the complex fault geometry could help evaluate the possibility of  
853 different rupture mechanisms using dynamic rupture simulations.

854

## 855 6. Conclusion

856

857 In this study, we conducted 3D dynamic rupture simulations for Cascadia using different  
858 interseismic locking models with a range of hypocenter locations in the South. While the  
859 locking models have similar static moments and locking distributions, their heterogeneous  
860 stress distribution leads to distinct rupture scenarios. Both Schmalzle and Li models  
861 demonstrate that the south is capable of generating  $M_w > 8$  segmented ruptures and full-margin  
862 ruptures depending on the frictional parameters and hypocenter locations. For instance, both  
863 segmented and full-margin ruptures can occur with the same hypocenter location given  
864 different frictional parameters.

865

866 We found that the heterogeneity of interseismic locking models plays a key role in determining  
867 the rupture process. The more heterogeneous Schmalzle locking model yields a stress  
868 distribution with more asperities, thus facilitating segmented ruptures on the high-stress  
869 asperities. These segmented ruptures appear to have a reasonable correlation with the  
870 along-strike extent of the inferred recurrence intervals. On the other hand, the more  
871 homogeneous Li locking model gives a smoother stress distribution, hence the scenarios are  
872 either full-margin ruptures or self-arrested ruptures. The selection of hypocenter location is  
873 also a crucial parameter in controlling the potential segmentation patterns. For the more  
874 heterogeneous model, the scenarios that initiated from the higher stress asperities demonstrate  
875 a significantly larger moment magnitude.

876

877 Accordingly, surface deformation is also largely controlled by these factors. While the  
878 homogeneous locking model results in a simpler coastal subsidence pattern with the largest  
879 subsidence in the region of highest slip and decreasing further away, the heterogeneous model  
880 gives a more complex pattern depending on the stress asperities. This also suggests that the  
881 A.D.1700 earthquake may represent a possibly more heterogeneous slip model provided its  
882 fluctuating coastal subsidence pattern. In particular, our results show that a three high-slip  
883 patches scenario can reproduce a reasonably similar seafloor deformation with the A.D. 1700  
884 earthquake. Apart from coastal subsidence, the synthetic ground shaking also demonstrates that

885 rupture directivity is strongly controlled by prescribed hypocenter locations, leading to nearly  
886 double the peak ground velocity for scenarios initiated at different hypocenter locations even  
887 though the resulting slip distributions are almost the same.

888

889 This project can be further developed from multiple perspectives in the future, including the  
890 off-fault plasticity, the along-strike changes in accretionary prism geometry, and the addition of  
891 splay faults. Our simulation results can also be applied to tsunami modeling to evaluate the  
892 tsunami risks for each segmented rupture type. Furthermore, our models may help evaluate the  
893 present probabilistic seismic hazard analysis (PSHA) by providing possible slip distributions of  
894 the paleoearthquakes for source characterization as well as the synthetic ground motions for  
895 comparison with that generated by the empirical ground motion prediction equations.

896

897 On top of specific investigations on Cascadia, our findings could help understand the general  
898 relationship between interseismic locking models and the possible earthquake slip patterns,  
899 thus the moment magnitudes. Our study together with the dynamic simulations for the other  
900 fault zones, such as the Nicoya Peninsula subduction megathrust (Yang et al., 2019a) and the  
901 Anninghe fault (Yao and Yang, 2022), raises the possibility to provide new insights into more  
902 efficient slip estimations of seismic potentials for the fault zones worldwide in the future.

903

#### 904 Data Availability Statement

905

906 All the data used in this work have been previously published, and references are provided in  
907 the paper. Dynamic rupture simulations were generated using the open-source software  
908 package PyLith, freely available at <https://github.com/geodynamics/pylith>. Locking model data  
909 may be found in the cited papers. All the important scripts and outputs are accessible in the  
910 temporal link  
911 [https://drive.google.com/drive/folders/1sGSr1tuyvgm\\_kHL9mslxsHzw1Lw3L2XX?usp=sharing](https://drive.google.com/drive/folders/1sGSr1tuyvgm_kHL9mslxsHzw1Lw3L2XX?usp=sharing)  
912 g during peer review. Upon acceptance of the manuscript, the data would be available in the  
913 CUHK Research Data Repository.

914

#### 915 Acknowledgments

916

917 We greatly appreciate Kelin Wang and Yajing Liu for their constructive comments on this  
918 study. Financial support is provided by the National Key R&D Program of China  
919 (2018YFC1503400), Hong Kong Research Grant Council Grants (14306119, 14306418),  
920 China Earthquake Science Experiment Project, CEA (grant no. 2018CSES0102), State Key  
921 Lab of Earthquake Dynamics (grant No. LED2021B03), The Open Foundation of the United  
922 Laboratory of Numerical Earthquake Forecasting (grant No. 2021LNEF02), CUHK Direct  
923 Grant from Faculty of Science.

924

## 925 7. References

926 Aagaard, B. T., Knepley, M. G., & Williams, C. A. (2013). A domain decomposition approach  
927 to implementing fault slip in finite-element models of quasi-static and dynamic crustal  
928 deformation. *Journal of Geophysical Research: Solid Earth*, *118*(6), 3059-3079.  
929 <https://doi.org/10.1002/jgrb.50217>

930 Aagaard, B., M. Knepley, C. Williams (2017a), PyLith v2.2.1 [software]. Davis, CA:  
931 Computational Infrastructure of Geodynamics. DOI: 10.5281/zenodo.886600,  
932 url: <https://geodynamics.org>

933 Aagaard, B., M. Knepley, C. Williams (2017b), PyLith Manual, Version 2.2.1, Computational  
934 Infrastructure for Geodynamics, Davis, CA,  
935 url: <https://geodynamics.org/resources/pylith/supportingdocs>

936 Atwater, B. F., & Hemphill-Haley, E. (1997). *Recurrence intervals for great earthquakes of the*  
937 *past 3,500 years at northeastern Willapa Bay, Washington* (No. 1576). US Government Printing  
938 Office. <https://doi.org/10.3133/pp1576>

939 Atwater, B. F., Carson, B., Griggs, G. B., Johnson, H. P., & Salmi, M. S. (2014). Rethinking  
940 turbidite paleoseismology along the Cascadia subduction zone. *Geology*, *42*(9), 827-830.  
941 <https://doi.org/10.1130/G35902.1>

942 Blacker, T. D., Owen, S. J., Staten, M. L., Quadros, W. R., Hanks, B., Clark, B. W., Meyers,  
943 R.J., Ernst, C., Merkley, K., Morris, R., McBride, C., Stimpson, C. J., Plooster, M., &  
944 Showman, S. (2016). *CUBIT geometry and mesh generation toolkit 15.1 user*

- 945 *documentation* (No. SAND-2016-1649R) [software]. Sandia National Lab.(SNL-NM),  
946 Albuquerque, NM (United States). <https://doi.org/10.2172/1430472>
- 947 Brocher, T. M. (2005). Empirical relations between elastic wavespeeds and density in the Earth's  
948 crust. *Bulletin of the seismological Society of America*, 95(6), 2081-2092.  
949 <https://doi.org/10.1785/0120050077>
- 950 Burgette, R. J., Weldon, R. J., & Schmidt, D. A. (2009). Interseismic uplift rates for western  
951 Oregon and along-strike variation in locking on the Cascadia subduction zone. *Journal of*  
952 *Geophysical Research: Solid Earth*, 114(B1). <https://doi.org/10.1029/2008JB005679>
- 953 Chen, X., & Yang, H. (2020). Effects of seismogenic width and low-velocity zones on  
954 estimating slip-weakening distance from near-fault ground deformation. *Geophysical Journal*  
955 *International*, 223(3), 1497-1510. <https://doi.org/10.1093/gji/ggaa385>
- 956 Day, S. M., Dalguer, L. A., Lapusta, N., & Liu, Y. (2005). Comparison of finite difference and  
957 boundary integral solutions to three-dimensional spontaneous rupture. *Journal of Geophysical*  
958 *Research: Solid Earth*, 110(B12). <https://doi.org/10.1029/2005JB003813>
- 959 Di Toro, G., Han, R., Hirose, T., De Paola, N., Nielsen, S., Mizoguchi, K., Ferri, F., Cocco, M.,  
960 and Shimamoto, T. (2011). Fault lubrication during earthquakes. *Nature*, 471(7339), 494-498.  
961 <https://doi.org/10.1038/nature09838>
- 962 Duan, B. (2012). Dynamic rupture of the 2011 Mw 9.0 Tohoku-Oki earthquake: Roles of a  
963 possible subducting seamount. *Journal of Geophysical Research: Solid Earth*, 117(B5).  
964 <https://doi.org/10.1029/2011JB009124>
- 965 Engelhart, S. E., Vacchi, M., Horton, B. P., Nelson, A. R., & Kopp, R. E. (2015). A sea-level  
966 database for the Pacific coast of central North America. *Quaternary Science Reviews*, 113, 78-92.  
967 <https://doi.org/10.1016/j.quascirev.2014.12.001>
- 968 Flück, P., Hyndman, R. D., & Wang, K. (1997). Three-dimensional dislocation model for great  
969 earthquakes of the Cascadia subduction zone. *Journal of Geophysical Research: Solid*  
970 *Earth*, 102(B9), 20539-20550. <https://doi.org/10.1029/97JB01642>

- 971 Frankel, A., Chen, R., Petersen, M., Moschetti, M., & Sherrod, B. (2015). 2014 update of the  
972 Pacific Northwest portion of the US National Seismic Hazard Maps. *Earthquake Spectra*,  
973 *31*(1\_suppl), S131-S148. <https://doi.org/10.1193/111314EQS193M>
- 974 Fujiwara, T., dos Santos Ferreira, C., Bachmann, A. K., Strasser, M., Wefer, G., Sun, T.,  
975 Kanamatsu, T., & Kodaira, S. (2017). Seafloor displacement after the 2011 Tohoku-Oki  
976 earthquake in the northern Japan trench examined by repeated bathymetric  
977 surveys. *Geophysical Research Letters*, *44*(23), 11-833.  
978 <https://doi.org/10.1002/2017GL075839>
- 979 Fukuyama, E., & Mikumo, T. (2007). Slip-weakening distance estimated at near-fault  
980 stations. *Geophysical research letters*, *34*(9). <https://doi.org/10.1029/2006GL029203>
- 981 Galvez, P., Ampuero, J. P., Dalguer, L. A., Somala, S. N., & Nissen-Meyer, T. (2014).  
982 Dynamic earthquake rupture modelled with an unstructured 3-D spectral element method  
983 applied to the 2011 M 9 Tohoku earthquake. *Geophysical Journal International*, *198*(2),  
984 1222-1240. <https://doi.org/10.1093/gji/ggu203>
- 985 Gao, D., Wang, K., Insua, T. L., Sypus, M., Riedel, M., & Sun, T. (2018). Defining megathrust  
986 tsunami source scenarios for northernmost Cascadia. *Natural Hazards*, *94*(1), 445-469.  
987 <https://doi.org/10.1007/s11069-018-3397-6>
- 988 Gao, X., and Wang, K. (2014). Strength of stick-slip and creeping subduction megathrusts  
989 from heat flow observations. *Science*, *345*(6200), 1038-1041.  
990 <https://doi.org/10.1126/science.1255487>
- 991 Gao, X., and Wang, K. (2017). Rheological separation of the megathrust seismogenic zone and  
992 episodic tremor and slip. *Nature*, *543*(7645), 416-419. <https://doi.org/10.1038/nature21389>
- 993 Goldfinger, C., Nelson, C.H., Morey, A.E., Johnson, J.R., Patton, J., Karabanov, E.,  
994 Gutierrez-Pastor, J., Eriksson, A.T., Gracia, E., Dunhill, G., Enkin, R.J., Dallimore, A., and  
995 Vallier, T., 2012, Turbidite event history—Methods and implications for Holocene  
996 paleoseismicity of the Cascadia subduction zone: U.S. Geological Survey Professional Paper  
997 1661–F, 170 p, 64 figures, available at <http://pubs.usgs.gov/pp/pp1661/f>
- 998 Goldfinger, C., Galer, S., Beeson, J., Hamilton, T., Black, B., Romsos, C., Patton, J., Nelson,  
999 C.H., Hausmann, R., & Morey, A. (2017). The importance of site selection, sediment supply,

- 1000 and hydrodynamics: A case study of submarine paleoseismology on the northern Cascadia  
1001 margin, Washington USA. *Marine Geology*, 384, 4-46.  
1002 <https://doi.org/10.1016/j.margeo.2016.06.008>
- 1003 Guatteri, M., & Spudich, P. (2000). What can strong-motion data tell us about slip-weakening  
1004 fault-friction laws?. *Bulletin of the Seismological Society of America*, 90(1), 98-116.  
1005 <https://doi.org/10.1785/0119990053>
- 1006 Han, S., Bangs, N. L., Carbotte, S. M., Saffer, D. M., and Gibson, J. C. (2017). Links between  
1007 sediment consolidation and Cascadia megathrust slip behaviour. *Nature Geoscience*, 10(12),  
1008 954-959. <https://doi.org/10.1038/s41561-017-0007-2>
- 1009 Harris, R. A., Barall, M., Aagaard, B., Ma, S., Roten, D., Olsen, K., Duan, B., Liu, D., Luo, B.,  
1010 Bai, K., Ampuero, J.P., Kaneko, Y., Gabriel, A.A., Duru, K., Ulrich, T., Wolherr, S., Shi, Z.,  
1011 Durham, E., Bydlon, S., Zhang, Z., Chen, X., Somala, S.N., Pelties, C., Tago, J., Cruz-Atienza,  
1012 V.M., Kozdon, J., Daub, E., Aslam, K., Kase, Y., Withers, K., and Dalguer, L. (2018). A suite  
1013 of exercises for verifying dynamic earthquake rupture codes. *Seismological Research*  
1014 *Letters*, 89(3), 1146-1162. <https://doi.org/10.1785/0220170222>
- 1015 Ida, Y. (1972). Cohesive force across the tip of a longitudinal-shear crack and Griffith's  
1016 specific surface energy. *Journal of Geophysical Research*, 77(20), 3796-3805.  
1017 <https://doi.org/10.1029/JB077i020p03796>
- 1018 Ide, S., & Aochi, H. (2013). Historical seismicity and dynamic rupture process of the 2011  
1019 Tohoku-Oki earthquake. *Tectonophysics*, 600, 1-13. <https://doi.org/10.1016/j.tecto.2012.10.018>
- 1020 Kelsey, H. M., Nelson, A. R., Hemphill-Haley, E., & Witter, R. C. (2005). Tsunami history of an  
1021 Oregon coastal lake reveals a 4600 yr record of great earthquakes on the Cascadia subduction  
1022 zone. *Geological Society of America Bulletin*, 117(7-8), 1009-1032.  
1023 <https://doi.org/10.1130/B25452.1>
- 1024 Lapusta, N., & Liu, Y. (2009). Three-dimensional boundary integral modeling of spontaneous  
1025 earthquake sequences and aseismic slip. *Journal of Geophysical Research: Solid*  
1026 *Earth*, 114(B9). <https://doi.org/10.1029/2008JB005934>

- 1027 Li, D., & Liu, Y. (2021). Cascadia megathrust earthquake rupture model constrained by geodetic  
1028 fault locking. *Philosophical Transactions of the Royal Society A*, 379(2196), 20200135.  
1029 <https://doi.org/10.1098/rsta.2020.0135>
- 1030 Li, S., Wang, K., Wang, Y., Jiang, Y., & Dosso, S. E. (2018). Geodetically inferred locking state  
1031 of the Cascadia megathrust based on a viscoelastic Earth model [dataset]. *Journal of*  
1032 *Geophysical Research: Solid Earth*, 123(9), 8056-8072. <https://doi.org/10.1029/2018JB015620>
- 1033 Li, Y., Song, X., Shan, X., Qu, C., & Wang, Z. (2016). Locking degree and slip rate deficit  
1034 distribution on MHT fault before 2015 Nepal Mw 7.9 earthquake. *Journal of Asian Earth*  
1035 *Sciences*, 119, 78-86. <https://doi.org/10.1016/j.jseae.2016.01.011>
- 1036 Lindsey, E. O., Mallick, R., Hubbard, J. A., Bradley, K. E., Almeida, R. V., Moore, J. D.,  
1037 Bürgmann, R., & Hill, E. M. (2021). Slip rate deficit and earthquake potential on shallow  
1038 megathrusts [dataset]. *Nature Geoscience*, 14(5), 321-326.  
1039 <https://doi.org/10.1038/s41561-021-00736-x>
- 1040 Long, A. J., & Shennan, I. (1998). Models of rapid relative sea-level change in Washington and  
1041 Oregon, USA. *The Holocene*, 8(2), 129-142. <https://doi.org/10.1191/095968398666306493>
- 1042 Materna, K., Bartlow, N., Wech, A., Williams, C., and Bürgmann, R. (2019). Dynamically  
1043 triggered changes of plate interface coupling in Southern Cascadia. *Geophysical Research*  
1044 *Letters*, 46(22), 12890-12899. <https://doi.org/10.1029/2019GL084395>
- 1045 McCaffrey, R., King, R. W., Payne, S. J., & Lancaster, M. (2013). Active tectonics of  
1046 northwestern US inferred from GPS-derived surface velocities. *Journal of Geophysical*  
1047 *Research: Solid Earth*, 118(2), 709-723. <https://doi.org/10.1029/2012JB009473>
- 1048 McCrory, P. A., Blair, J. L., Oppenheimer, D. H., & Walter, S. R. (2004). Depth to the Juan de  
1049 Fuca slab beneath the Cascadia subduction margin: A 3-D model for sorting earthquakes  
1050 [dataset]. <https://doi.org/10.3133/ds91>
- 1051 Michel, S., Avouac, J. P., Lapusta, N., & Jiang, J. (2017). Pulse-like partial ruptures and high-  
1052 frequency radiation at creeping-locked transition during megathrust earthquakes. *Geophysical*  
1053 *Research Letters*, 44(16), 8345-8351. <https://doi.org/10.1002/2017GL074725>

- 1054 Michel, S., Gualandi, A., and Avouac, J. P. (2019). Interseismic coupling and slow slip events on  
1055 the Cascadia megathrust. *Pure and Applied Geophysics*, 176(9), 3867-3891.  
1056 <https://doi.org/10.1007/s00024-018-1991-x>
- 1057 Mikumo, T., Olsen, K. B., Fukuyama, E., & Yagi, Y. (2003). Stress-breakdown time and  
1058 slip-weakening distance inferred from slip-velocity functions on earthquake faults. *Bulletin of*  
1059 *the Seismological Society of America*, 93(1), 264-282. <https://doi.org/10.1785/0120020082>
- 1060 Moreno, M., Rosenau, M., and Oncken, O. (2010). 2010 Maule earthquake slip correlates with  
1061 pre-seismic locking of Andean subduction zone. *Nature*, 467(7312), 198-202.  
1062 <https://doi.org/10.1038/nature09349>
- 1063 Nur, A. (1978). Nonuniform friction as a physical basis for earthquake mechanics. *pure and*  
1064 *applied geophysics*, 116(4), 964-989. <https://doi.org/10.1007/BF00876550>
- 1065 Petersen, M.D., Moschetti, M.P., Powers, P.M., Mueller, C.S., Haller, K.M., Frankel, A.D.,  
1066 Zeng, Yuehua, Rezaeian, Sanaz, Harmsen, S.C., Boyd, O.S., Field, Ned, Chen, Rui, Rukstales,  
1067 K.S., Luco, Nico, Wheeler, R.L., Williams, R.A., and Olsen, A.H. (2014), Documentation for  
1068 the 2014 update of the United States national seismic hazard maps: U.S. Geological Survey  
1069 Open-File Report 2014–1091, 243 p., <http://dx.doi.org/10.3133/ofr20141091>
- 1070 Pollitz, F. F., & Evans, E. L. (2017). Implications of the earthquake cycle for inferring fault  
1071 locking on the Cascadia megathrust. *Geophysical Journal International*, 209(1), 167-185.  
1072 <https://doi.org/10.1093/gji/ggx009>
- 1073 Priest, G. R., Goldfinger, C., Wang, K., Witter, R. C., Zhang, Y., & Baptista, A. M. (2009).  
1074 Tsunami hazard assessment of the Northern Oregon coast: a multi-deterministic approach  
1075 tested at Cannon Beach, Clatsop County, Oregon. *Oregon Department of Geology Mineral*  
1076 *Industries Special Paper*, 41, 87.
- 1077 Ramos, M. D., Huang, Y., Ulrich, T., Li, D., Gabriel, A. A., & Thomas, A. M. (2021). Assessing  
1078 margin-wide rupture behaviors along the Cascadia megathrust with 3-D dynamic rupture  
1079 simulations. *Journal of Geophysical Research: Solid Earth*, 126(7), e2021JB022005.  
1080 <https://doi.org/10.1029/2021JB022005>

- 1081 Rogers, G., & Dragert, H. (2003). Episodic tremor and slip on the Cascadia subduction zone:  
1082 The chatter of silent slip. *science*, 300(5627), 1942-1943.  
1083 <https://doi.org/10.1126/science.1084783>
- 1084 Rowe, C. D., & Griffith, W. A. (2015). Do faults preserve a record of seismic slip: A second  
1085 opinion. *Journal of Structural Geology*, 78, 1-26. <https://doi.org/10.1016/j.jsg.2015.06.006>
- 1086 Saffer, D. M., & Tobin, H. J. (2011). Hydrogeology and mechanics of subduction zone  
1087 forearcs: Fluid flow and pore pressure. *Annual Review of Earth and Planetary Sciences*, 39,  
1088 157-186. <https://doi.org/10.1146/annurev-earth-040610-133408>
- 1089 Satake, K., Wang, K., & Atwater, B. F. (2003). Fault slip and seismic moment of the 1700  
1090 Cascadia earthquake inferred from Japanese tsunami descriptions. *Journal of Geophysical*  
1091 *Research: Solid Earth*, 108(B11). <https://doi.org/10.1029/2003JB002521>
- 1092 Schmalzle, G. M., McCaffrey, R., & Creager, K. C. (2014). Central Cascadia subduction zone  
1093 creep [dataset]. *Geochemistry, Geophysics, Geosystems*, 15(4), 1515-1532.  
1094 <https://doi.org/10.1002/2013GC005172>
- 1095 Stanislawski, K., Roesner, A., and Ikari, M. J. (2022). Implications for megathrust slip  
1096 behavior and pore pressure at the shallow northern Cascadia subduction zone from laboratory  
1097 friction experiments. *Earth and Planetary Science Letters*, 578, 117297.  
1098 <https://doi.org/10.1016/j.epsl.2021.117297>
- 1099 Stephenson, W. J., Reitman, N. G., & Angster, S. J. (2017). *P-and S-wave velocity models*  
1100 *incorporating the Cascadia subduction zone for 3D earthquake ground motion simulations,*  
1101 *Version 1.6—Update for Open-File Report 2007–1348* (No. 2017-1152). US Geological Survey.  
1102 <https://doi.org/10.3133/ofr20171152>
- 1103 Tinti, E., Fukuyama, E., Piatanesi, A., & Cocco, M. (2005). A kinematic source-time function  
1104 compatible with earthquake dynamics. *Bulletin of the Seismological Society of America*, 95(4),  
1105 1211-1223. <https://doi.org/10.1785/0120040177>
- 1106 Tréhu, A. M., Blakely, R. J., & Williams, M. C. (2012). Subducted seamounts and recent  
1107 earthquakes beneath the central Cascadia forearc. *Geology*, 40(2), 103-106.  
1108 <https://doi.org/10.1130/G32460.1>

- 1109 Ulrich, T., Gabriel, A. A., & Madden, E. H. (2022). Stress, rigidity and sediment strength  
1110 control megathrust earthquake and tsunami dynamics. *Nature Geoscience*, 1-7.  
1111 <https://doi.org/10.1038/s41561-021-00863-5>
- 1112 Walton, M.A., Staisch, L.M., Dura, T., Pearl, J.K., Sherrod, B., Gomberg, J., Engelhart, S.,  
1113 Tréhu, A., Watt, J., Perkins, J., Witter, R.C., Bartlow, N., Goldfinger, C., Kelsey, H., Morey,  
1114 A.E., Sahakian, V.J., Tobin, H., Wang, K., Wells, R., & Wirth, E. (2021). Toward an  
1115 Integrative Geological and Geophysical View of Cascadia Subduction Zone Earthquakes.  
1116 *Annual Review of Earth and Planetary Sciences*, 49, 367-398.  
1117 <https://doi.org/10.1146/annurev-earth-071620-065605>
- 1118 Wang, K., Wells, R., Mazzotti, S., Hyndman, R. D., & Sagiya, T. (2003). A revised dislocation  
1119 model of interseismic deformation of the Cascadia subduction zone. *Journal of Geophysical*  
1120 *Research: Solid Earth*, 108(B1). <https://doi.org/10.1029/2001JB001227>
- 1121 Wang, K., & Dixon, T. (2004). “Coupling” semantics and science in earthquake research. *Eos*,  
1122 *Transactions American Geophysical Union*, 85(18), 180-180.  
1123 <https://doi.org/10.1029/2004EO180005>
- 1124 Wang, K. (2007). 17. Elastic and Viscoelastic Models of Crustal Deformation in Subduction  
1125 Earthquake Cycles. In *The seismogenic zone of subduction thrust faults* (pp. 540-575).  
1126 Columbia University Press. <https://doi.org/10.7312/dixo13866-017>
- 1127 Wang, K., Hu, Y., & He, J. (2012). Deformation cycles of subduction earthquakes in a  
1128 viscoelastic Earth. *Nature*, 484(7394), 327-332. <https://doi.org/10.1038/nature11032>
- 1129 Wang, K., & Tréhu, A. M. (2016). Invited review paper: Some outstanding issues in the study  
1130 of great megathrust earthquakes—The Cascadia example. *Journal of Geodynamics*, 98, 1-18.  
1131 <https://doi.org/10.1016/j.jog.2016.03.010>
- 1132 Wang, P. L., Engelhart, S. E., Wang, K., Hawkes, A. D., Horton, B. P., Nelson, A. R., & Witter,  
1133 R. C. (2013). Heterogeneous rupture in the great Cascadia earthquake of 1700 inferred from  
1134 coastal subsidence estimates. *Journal of Geophysical Research: Solid Earth*, 118(5),  
1135 2460-2473. <https://doi.org/10.1002/jgrb.50101>

- 1136 Watt, J. T., & Brothers, D. S. (2021). Systematic characterization of morphotectonic variability  
1137 along the Cascadia convergent margin: Implications for shallow megathrust behavior and  
1138 tsunami hazards. *Geosphere*, 17(1), 95-117. <https://doi.org/10.1130/GES02178.1>
- 1139 Wells, D. L., & Coppersmith, K. J. (1994). New empirical relationships among magnitude,  
1140 rupture length, rupture width, rupture area, and surface displacement. *Bulletin of the*  
1141 *seismological Society of America*, 84(4), 974-1002. <https://doi.org/10.1785/BSSA0840040974>
- 1142 Weng, H., & Ampuero, J. P. (2020). Continuum of earthquake rupture speeds enabled by  
1143 oblique slip. *Nature Geoscience*, 13(12), 817-821. <https://doi.org/10.1038/s41561-020-00654-4>
- 1144 Weng, H., & Yang, H. (2018). Constraining frictional properties on fault by dynamic rupture  
1145 simulations and near-field observations. *Journal of Geophysical Research: Solid Earth*, 123(8),  
1146 6658-6670. <https://doi.org/10.1029/2017JB015414>
- 1147 Wilson, A., & Ma, S. (2021). Wedge plasticity and fully coupled simulations of dynamic  
1148 rupture and tsunami in the Cascadia subduction zone. *Journal of Geophysical Research: Solid*  
1149 *Earth*, 126(7), e2020JB021627. <https://doi.org/10.1029/2020JB021627>
- 1150 Witter, R. C., Zhang, Y., Wang, K., Goldfinger, C., Priest, G. R., & Allan, J. C. (2012).  
1151 Coseismic slip on the southern Cascadia megathrust implied by tsunami deposits in an Oregon  
1152 lake and earthquake-triggered marine turbidites. *Journal of Geophysical Research: Solid*  
1153 *Earth*, 117(B10). <https://doi.org/10.1029/2012JB009404>
- 1154 Yang, H., Yao, S., He, B., Newman, A. V., & Weng, H. (2019a). Deriving rupture scenarios  
1155 from interseismic locking distributions along the subduction megathrust. *Journal of*  
1156 *Geophysical Research: Solid Earth*, 124(10), 10376-10392.  
1157 <https://doi.org/10.1029/2019JB017541>
- 1158 Yang, H., Yao, S., He, B., & Newman, A. V. (2019b). Earthquake rupture dependence on  
1159 hypocentral location along the Nicoya Peninsula subduction megathrust. *Earth and Planetary*  
1160 *Science Letters*, 520, 10-17. <https://doi.org/10.1016/j.epsl.2019.05.030>
- 1161 Yao, S., & Yang, H. (2020). Rupture dynamics of the 2012 Nicoya Mw 7.6 earthquake:  
1162 Evidence for low strength on the megathrust. *Geophysical Research Letters*, 47(13),  
1163 e2020GL087508. <https://doi.org/10.1029/2020GL087508>

1164 Yao, S., & Yang, H. (2022). Hypocentral dependent shallow slip distribution and rupture  
1165 extents along a strike-slip fault. *Earth and Planetary Science Letters*, 578, 117296.  
1166 <https://doi.org/10.1016/j.epsl.2021.117296>

## **Dynamic Rupture Scenarios of the Cascadia Megathrust based on Interseismic Locking Models**

Yuk Po Bowie Chan<sup>1</sup>, Suli Yao<sup>1</sup>, Hongfeng Yang<sup>1,2</sup>

<sup>1</sup>Earth and Environmental Sciences Programme, The Chinese University of Hong Kong, Hong Kong, China, <sup>2</sup>Shenzhen Research Institute, The Chinese University of Hong Kong, Shenzhen, China

### **Contents of this file**

Figures S1 to S6  
Movies S1 to S7

### **Introduction**

This supporting document explains the parameters used in the study and extends the results of the dynamic simulations. Specifically, Figure S1 shows the velocity models of the continental and oceanic blocks of Cascadia. Figure S2 is the comparison between dynamic simulations using bi-material (continental and oceanic) and 1D depth-dependent (only continental) material properties, illustrating the little difference between these two material assumptions. Figure S3 shows the dynamic simulation results assuming different thicknesses for the frontal prism. Figure S4 demonstrates the location of the sediment deposition at different depths, justifying our choice of the frontal prism depth range from 5 – 7 km. Figure S5 shows the moment magnitude of dynamic simulations initiated from different hypocenter locations with 10 km and 15 km radius nucleation zones, supporting our choice of 15 km radius nucleation zones. Figure S6 extends the Schmalzle-based dynamic simulations to a  $dc$  of 1 m.

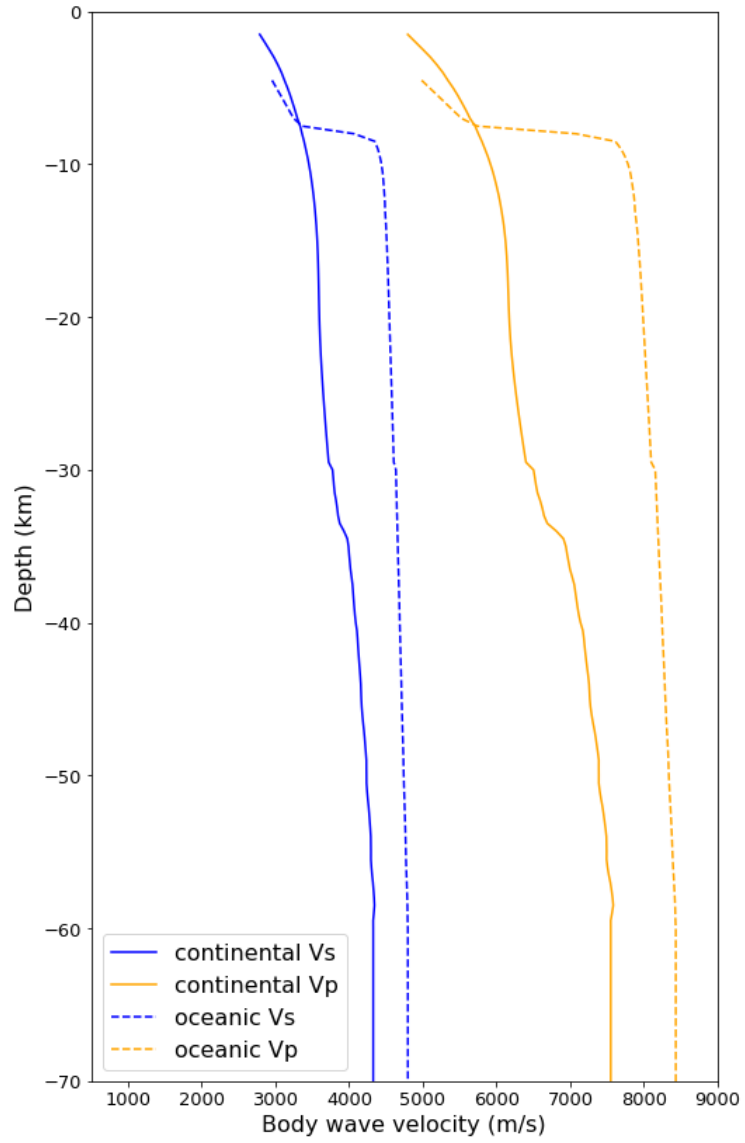


Figure S1. Velocity models of continental and oceanic blocks for Cascadia (Stephenson et al., 2017).

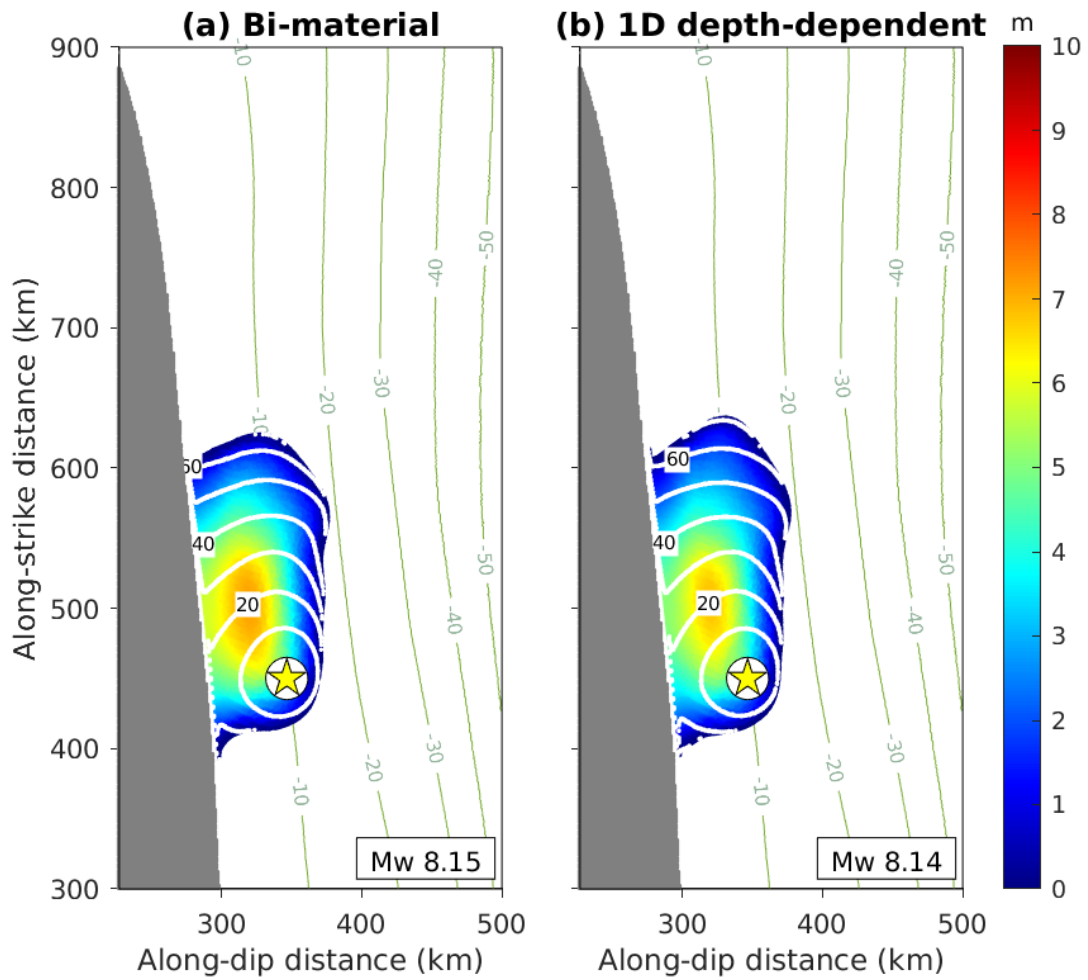


Figure S2. Final slip distribution of the same stress field utilizing (a) bi-material materials properties where the velocity contrast across two blocks is around 30%, and (a) 1D depth-dependent material properties (Figure 3a).

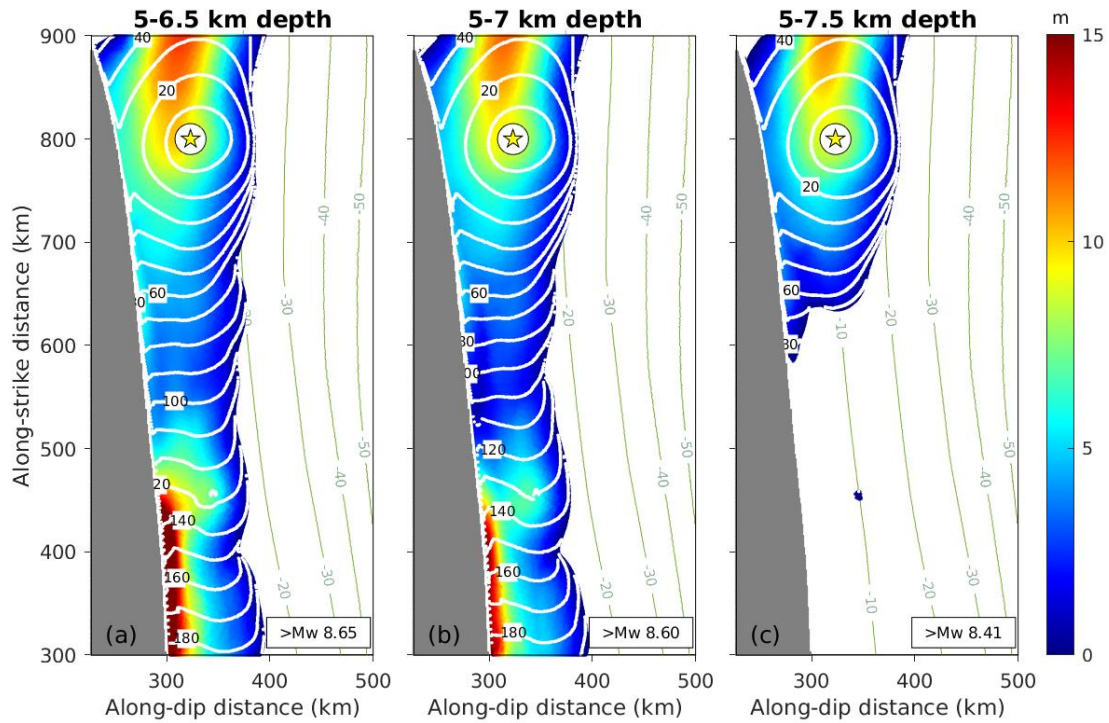


Figure S3. Final slip distribution derived from the Schmalzle model using a  $dc$  of 1 m assuming different thicknesses of the frontal prism. Stars: hypocenter locations. Olive-green contours: slab depth contours. Rupture fronts (white contours) are displayed every 10 seconds and numbered every 20 seconds. (a) Accretionary prism from 6.5 km depth to trench (5 km depth). Strong free-surface reflections are generated near the trench, causing an unphysical final slip that exceeds the slip deficit (b) From 5-7 km depth - our model assumption. (c) From 5 – 7.5 km depth.

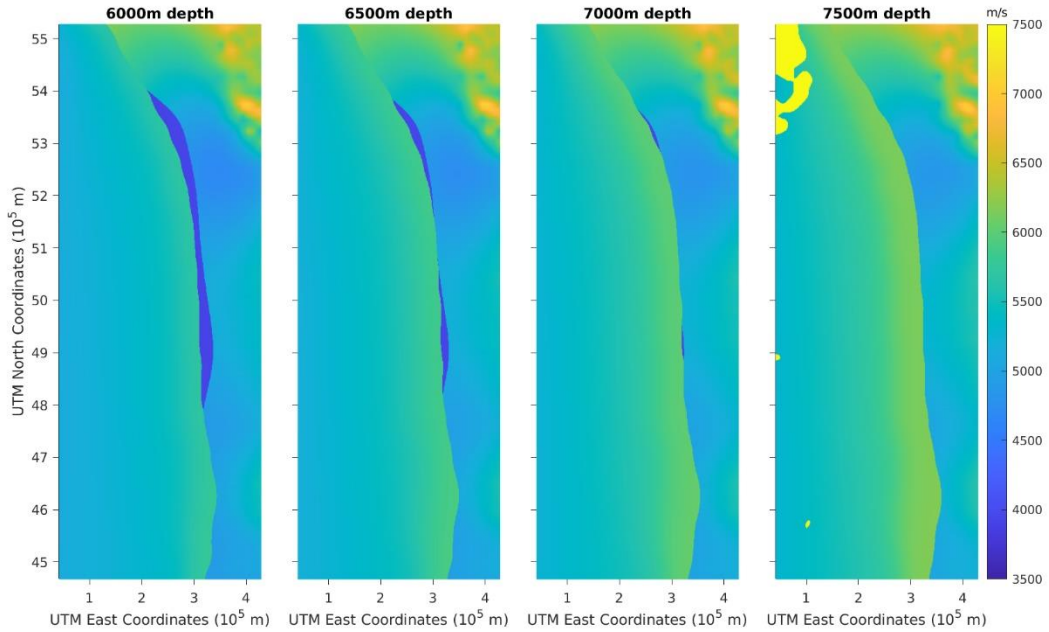


Figure S4. P wave velocity cross-sections of CSZ at different depths (Stephenson et al., 2017). The sediment deposition / accretionary prism is shown as the central gap with low velocity.

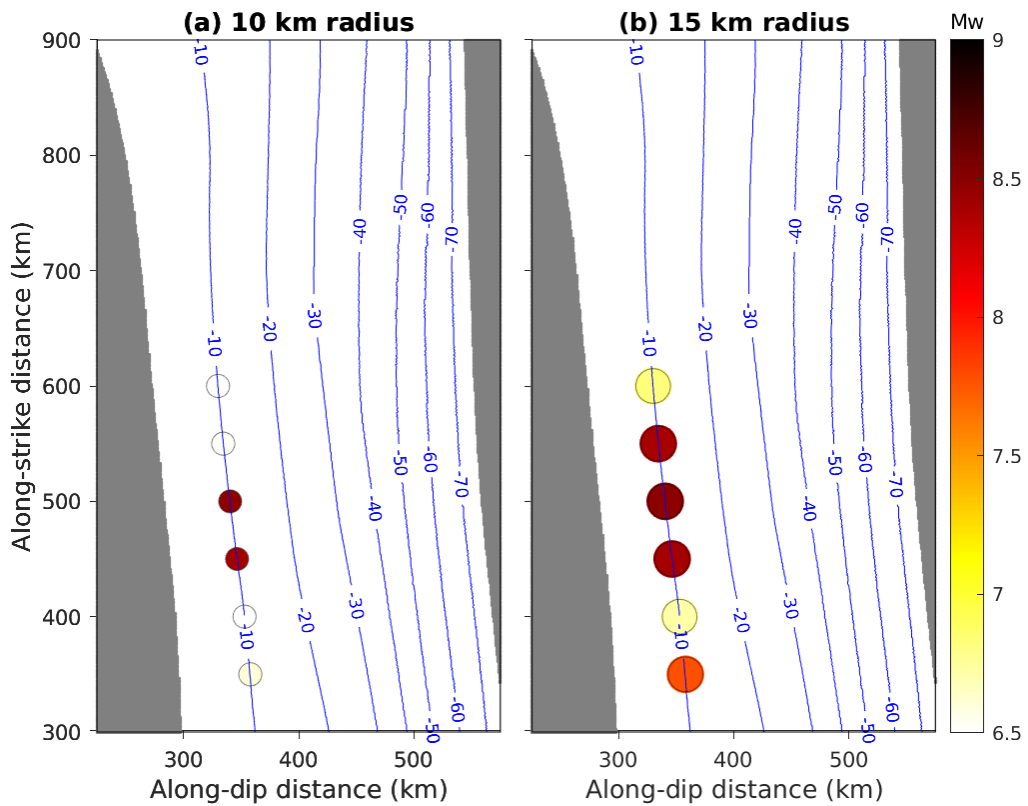


Figure S5. Map view of the moment magnitudes of rupture scenarios nucleated at each location (circles) using (a) 10 km radius and (b) 15 km radius nucleation zones.

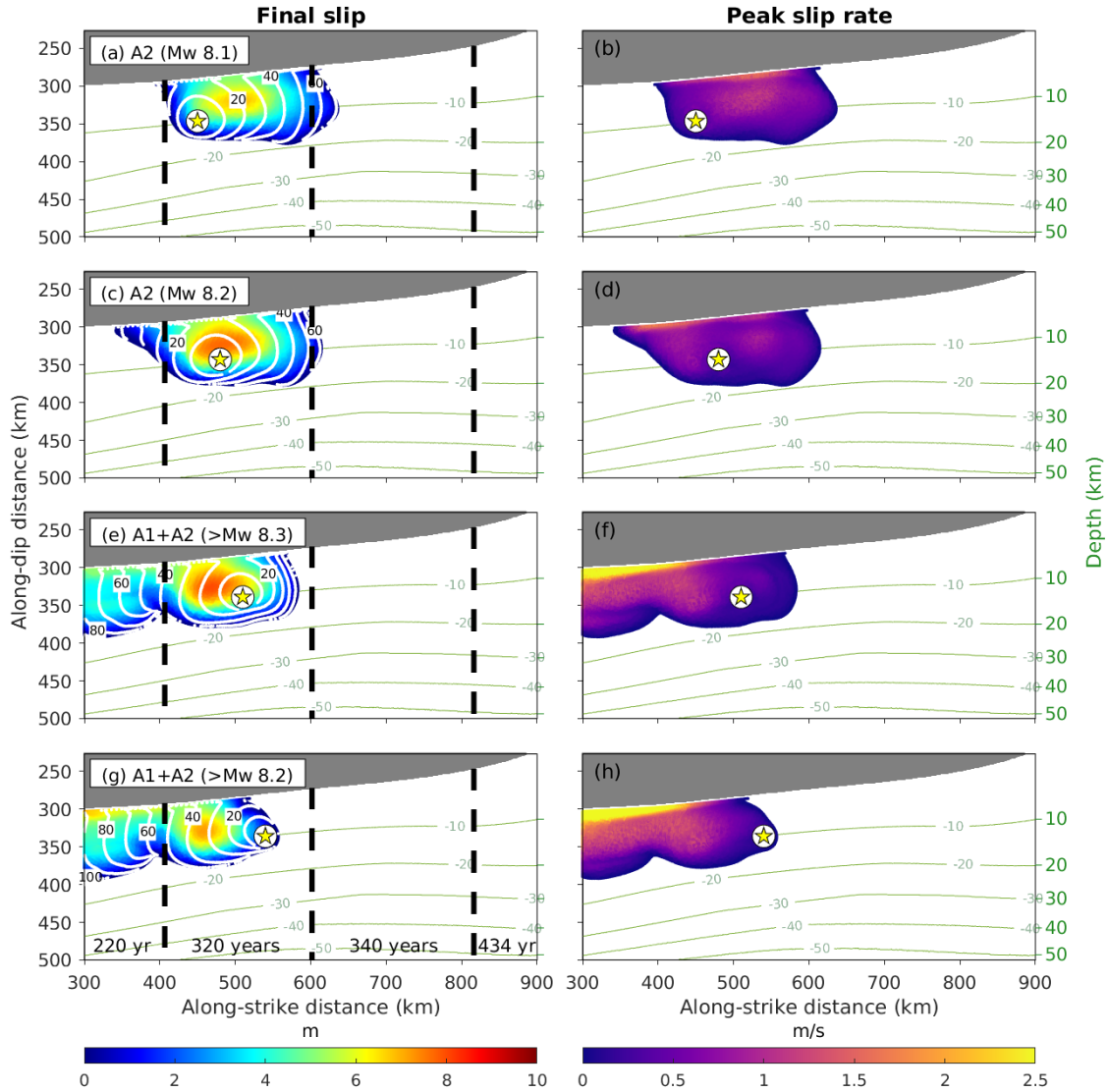


Figure S6. Same as Figure 6, except using a  $dc$  of 1 m. (a) & (b) Scenario rupturing the A1 asperity. (c) & (d) Scenario rupturing A1 and A2 asperities.

#### Supplementary Movies: Slip rate evolution in dynamic rupture scenarios

- S1: Schmalzle model–FMR initiated from A1 (Figure 6e)
- S2: Schmalzle model–FMR initiated from A2 (Figure 6g)
- S3: Li model–FMR initiated at 15 km depth (Figure 7c)
- S4: Li model–FMR initiated at 10 km depth (Figure 7e)
- S5: Schmalzle model–A1+A2+C event (Figure 6c)
- S6: Schmalzle model–A1 event (Figure 6a)
- S7: Li model–segmented rupture (Figure 7a)